Deformation bands in the Etchegoin Formation sandstone: Triaxial deformation experiments and implications for principle stress directions in central California

Peter C. Lindquist
Senior Integrative Exercise
9 March 2018

Submitted in partial fulfillment of the requirements for a
Bachelor of Arts degree from Carleton College, Northfield, Minnesota.

Table of Contents

Deformation bands in the Etchegoin Formation sandstone: Triaxial deformation experiments and implications for principle stress directions in central California

Peter C. Lindquist
Senior Integrative Exercise
9 March 2018

Advisors:
Dr. Sarah J. Titus
Department of Geology, Carleton College, Northfield, MN

Dr. Melodie E. French
Department of Earth, Environmental, and Planetary Sciences, Rice University, Houston, TX

ABSTRACT

I present structural measurements of deformation bands in the Miocene-Pliocene Etchegoin Formation of central California collected at several sites spanning four large-scale folds northeast of Parkfield, CA. From these data, I infer the direction of maximum horizontal compressive stress (S_{Hmax}) by bisecting the acute angle between sets of conjugate sets of deformation bands—a common pattern across the field area. These S_{Hmax} measurements, at 60°-70° to the strike of the San Andreas fault, are at odds with values reported by the World Stress Map, which generally form high angles (>80°) with the strike of the San Andreas fault. Because of this discrepancy and the potential for deformation bands to serve as an indicator of regional stress patterns in central California, I use triaxial deformation experiments on samples of Etchegoin Formation sandstone to better understand how deformation bands form in response to applied stresses.

I investigate the impact of varying bedding direction and the amount of axial strain on experimentally deformed samples. At the low effective confining pressures (5-20 MPa) used in this study, no localized features are observed in the deformed samples for any amount of applied axial strain (2-10%). Analysis of thin sections made from deformed cores confirm that deformation is distributed throughout the samples in grain fracturing and pore space collapse. Although the results of these experiments are not instructive for inferring stress directions from natural deformation bands, they are a step towards understanding how the Etchegoin Formation deforms and provide some direction for future triaxial experiments.

Keywords: deformation bands; triaxial tests; San Andreas fault; central California; rock mechanics; stress

INTRODUCTION

The San Andreas fault system constitutes the boundary between the Pacific plate and the Sierra Nevada-Great Valley block and accommodates transpressional deformation between these two crustal units (Argus and Gordon, 2001). In addition to the right-lateral strike-slip motion accommodated by the San Andreas fault itself, convergent and transverse motion between the Pacific plate and Sierra Nevada-Great Valley block is distributed among off-fault structures (Teyssier et al., 1995). The frictional strength of the San Andreas fault and whether it is a strong fault or weak fault has been debated over decades (e.g., Brune et al., 1969; Zoback et al., 1987; Scholz, 2000; Townend and Zoback, 2001). The strength of the San Andreas fault is an important control on the state of stress in the surrounding crust, including the directions of principle stresses (Zoback et al., 1987; Hardebeck and Micheal, 2004). Measurements of the direction of maximum horizontal compressive stress (S_{Hmax}) are therefore an important dataset for constraining the strength of the San Andreas fault. Furthermore, the directions of principle stresses have implications for how strain is partitioned between the San Andreas Fault and its borderlands and contributes to our understanding of seismic hazards in the region (Lettis and Hanson, 1991).

To the northeast of the San Andreas fault in central California, plate-boundary deformation is accommodated in folds and faults up to 40 km away (Namson and Davis, 1988). In this region, data from the World Stress Map commonly indicate that S_{Hmax} is directed at high angles (>80°) to the strike of the San Andreas fault—an observation that has been used to support the weak-fault model of the San Andreas fault (Fig. 1; e.g., Zoback et al., 1987; Townend and Zoback, 2004). However, results from previous field

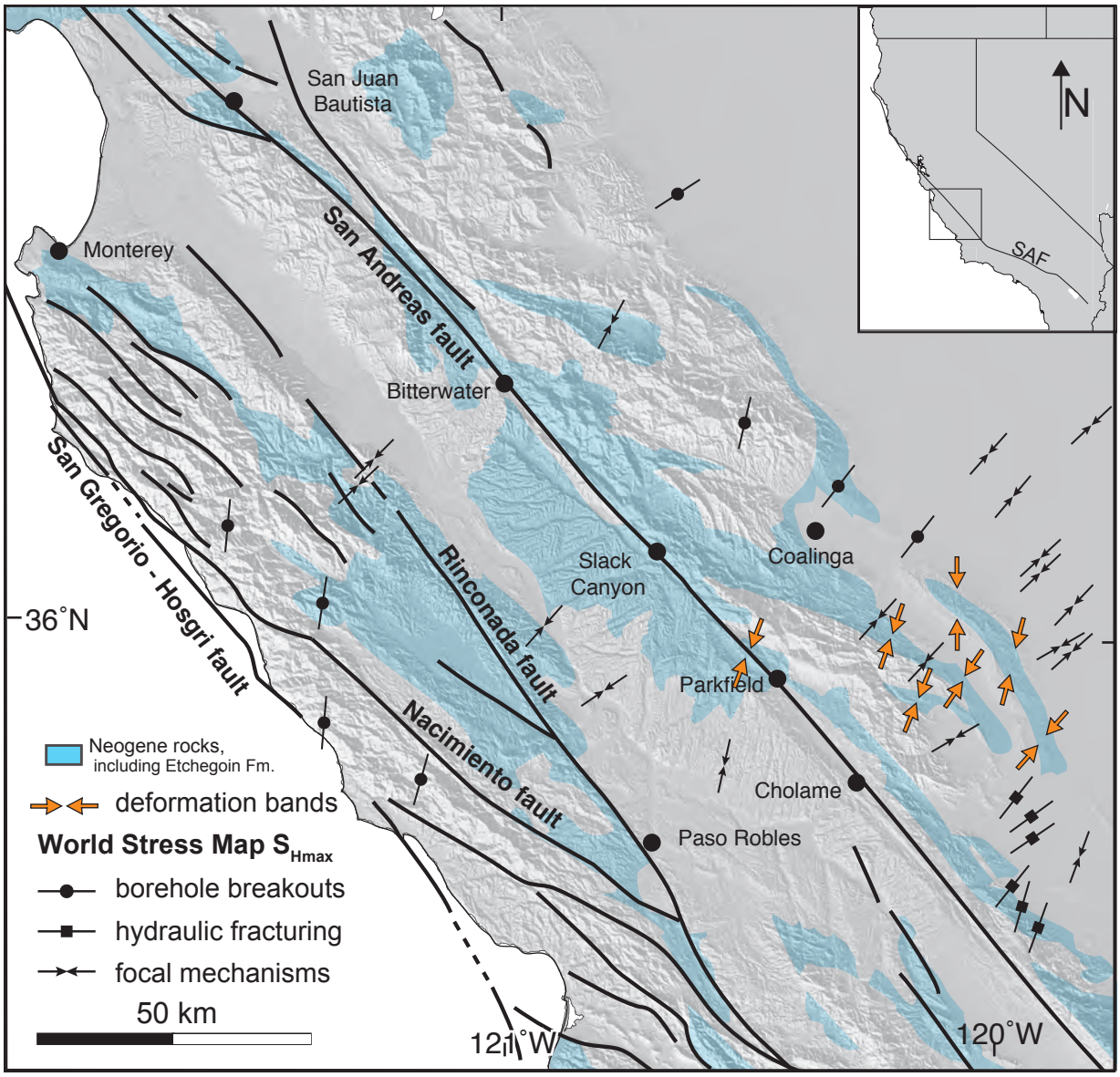

Figure 1. Map of central California showing major faults and S_{Hmax} directions from the World Stress Map (black symbols), which commonly form high angles with the strike of the San Andreas fault, and those inferred from deformation band directions (orange). Highlighted blue areas show the distribution of Neogene, primarily marine, sediments including the Etchegoin Formation near the field sites studied here. World Stress Map data are from Heidbach et al., 2008.

work in which I have been involved imply contradictory S_{Hmax} directions. This work, which has focused on making structural measurements of deformation bands in outcrops near Parkfield, CA, suggests that S_{Hmax} is directed at more moderate angles (60°-70°) to the strike of the San Andreas fault (Livesay et al., 2013; Lindquist et al., 2016). Deformation bands—tabular strain localization features that commonly develop in porous granular materials (Fossen et al., 2007)—are prevalent in much of the blue sandstones of the upper Miocene-lower Pliocene Etchegoin Formation that crops out in several folds up to 30 km to the northeast of Parkfield, CA (Fig. 1). The use of these small-scale structures that occur over a broad geographic area northeast of the San Andreas fault may provide a valuable supplement and check for those measurements reported in the World Stress Map. I will present here the data from these previous field efforts, as well as my interpretations of the principle stresses indicated by these data.

The model I use to make S_{Hmax} interpretations from deformation band directions is chosen because the observed geometric pattern formed by deformation bands in the field (i.e., a conjugate set of conjugate sets) matches what might be expected in the three-dimensional stress regime of the faulting model developed by Reches (1983). In order to test this assumption of how deformation bands record principle stress directions in the Etchegoin Formation, I conducted a suite of triaxial deformation experiments on samples of Etchegoin Formation sandstone. The triaxial tests simulate both burial and application of tectonic stress to an undeformed core of sandstone. The former is achieved by applying confining and pore fluid pressures, and for the latter, a differential stress—that is, the difference between maximum and minimum compressive stresses ($\sigma_1 - \sigma_3$)—is applied to the sample with an axial piston. A total of six triaxial experiments were

conducted to different magnitudes of axial strain. Although the original goal of these experiments was to reproduce deformation bands in the laboratory and measure their orientation with respect to the maximum compressive stress, no deformation bands localized in the experimental samples. The mechanical data collected during these experiments and post-test analysis of thin sections of the samples are presented here after an introduction to deformation bands and their significance in central California.

THE SAN ANDREAS FAULT SYSTEM IN CENTRAL CALIFORNIA

Deformation in the San Andreas fault system is partitioned between the San Andreas fault and off-fault structures, such as folds and faults that accommodate both fault-perpendicular and fault-parallel deformation (Teyssier et al., 1995; Titus et al, 2011) as a result of the oblique convergence between the Pacific plate and the Sierra Nevada-Great Valley block (Argus and Gordon, 2001). Near Parkfield, California, the San Andreas fault transitions from a locked segment—in which stress builds up and is released in earthquakes—to a creeping segment—in which right-lateral strike-slip motion occurs via aseismic creep. The rate of strike-slip motion varies along the creeping section from 21–26 mm yr^{-1} (Titus et al., 2006), while fault-perpendicular convergence along the creeping section occurs at a rate of 3.2 ± 1.4 mm yr^{-1} (Argus and Gordon, 2001). To the northeast of the San Andreas fault in central California, associated off-fault deformation is expressed up to ~50 km away in folds and faults in the Franciscan Assemblage and Mesozoic-early Cenozoic Great Valley Sequence basement rock, and overlying Cenozoic sedimentary strata (Bartow, 1988). Some of this deformation occurs within Pliocene and

younger rocks, indicating recent deformation of the San Andreas fault borderlands (e.g., Harding, 1976; Medwedeff, 1989; Bloch et al., 1993; Titus et al., 2011).

The direction of S_{Hmax} in central California has previously been inferred from several datasets including borehole breakouts, earthquake focal mechanism inversions, and fold axis orientations (e.g., Mount and Suppe, 1987; Zoback et al., 1987; Hardebeck and Hauksson, 1999; Hardebeck and Michael, 2004; Townend and Zoback, 2004). Data from the World Stress Map show that S_{Hmax} is directed at high angles (>80°) to the strike of the San Andreas fault in central California (Fig. 1). These high angle S_{Hmax} measurements have been used to support the hypothesis that the San Andreas fault is a weak fault with low resolved shear stresses (e.g., Mount and Suppe, 1987; Zoback, 1987). In the weak-fault model, the low frictional strength of the material along the San Andreas fault implies that shear stresses on the fault plane will be low (Mount and Suppe, 1987). As a result, the direction of maximum compressive stress acting on the San Andreas fault should be at a high angle relative to the strike of the fault to minimize the shear stress on the fault (Hardebeck and Michael, 2004).

Some authors, however, use similar data to infer intermediate angles (~60° to 70°; e.g., Hardebeck and Michael, 2004), or even low angles (~45°, e.g., Scholz, 2000), between S_{Hmax} and the strike of the San Andreas fault. Contrary to the weak fault model, these measurements would support a San Andreas fault capable of accommodating higher shear stresses – i.e., a strong fault with a coefficient of friction along the fault plane comparable to that generally expected of crustal materials (Hardebeck and Michael, 2004). Because of the discrepancy between these interpretations, further investigation of regional stresses on the San Andreas fault would benefit from the study of other,

independent records of stress in central California. Field measurements of deformation band directions may provide one such method.

DEFORMATION BANDS

Deformation bands have been studied in various geologic contexts since Aydin (1978), and have been observed in materials ranging from well-lithified sandstones to unconsolidated sediments. These strain localization structures only occur in such porous, granular materials (Aydin and Johnson, 1983; Fossen et al., 2007), and may result from tectonic deformation, or soft sediment deformation and burial (e.g., Jamison and Stearns, 1983; Fossen et al., 2007; Ballas et al., 2013). In the field, deformation bands appear in outcrop as resistant features that stand in relief against the host rock, and sometimes develop in large zones of many deformation bands, which may ultimately fail by the development of a through-going fault (Fig. 2; e.g., Aydin and Johnson, 1978; Fossen et al., 2007). Individual deformation bands have mm-scale thicknesses, and are often traceable for tens of meters. Deformation bands develop in several styles depending on the stress conditions controlling deformation, exhibiting either compactional behavior, dilational behavior, shear behavior, or some combination of both shear and compaction or shear and dilation (Fig. 3; Schultz and Siddharthan, 2005; Fossen et al., 2007). Shear bands will display mm- to cm-scale offsets, and may exhibit decreased grain size relative to the host rock as a result of cataclasis (e.g., Jamison and Stearns, 1983). Porosity in compactional bands will also be reduced relative to the host rock, whereas dilation bands show increased porosity (e.g., Alikarami and Torabi, 2015). Although the term deformation band describes all these various types of tabular strain localization in porous

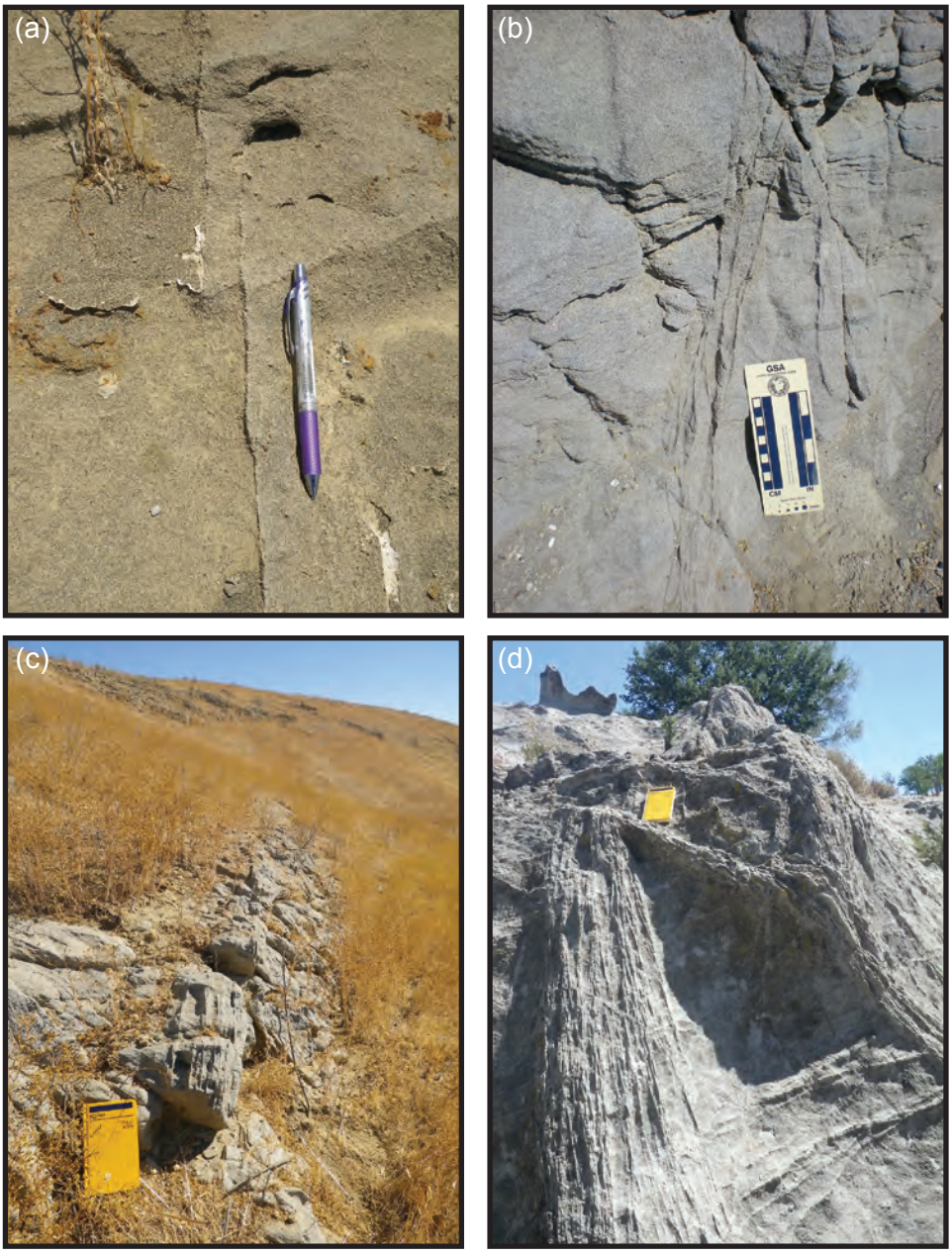

Figure 2. The various styles of deformation bands observed in central California: (a) single bands, (b) clusters of 2-5 bands, (c) zones of bands, (d) zones of bands cross-cutting other zones, potentially with through-going faults.

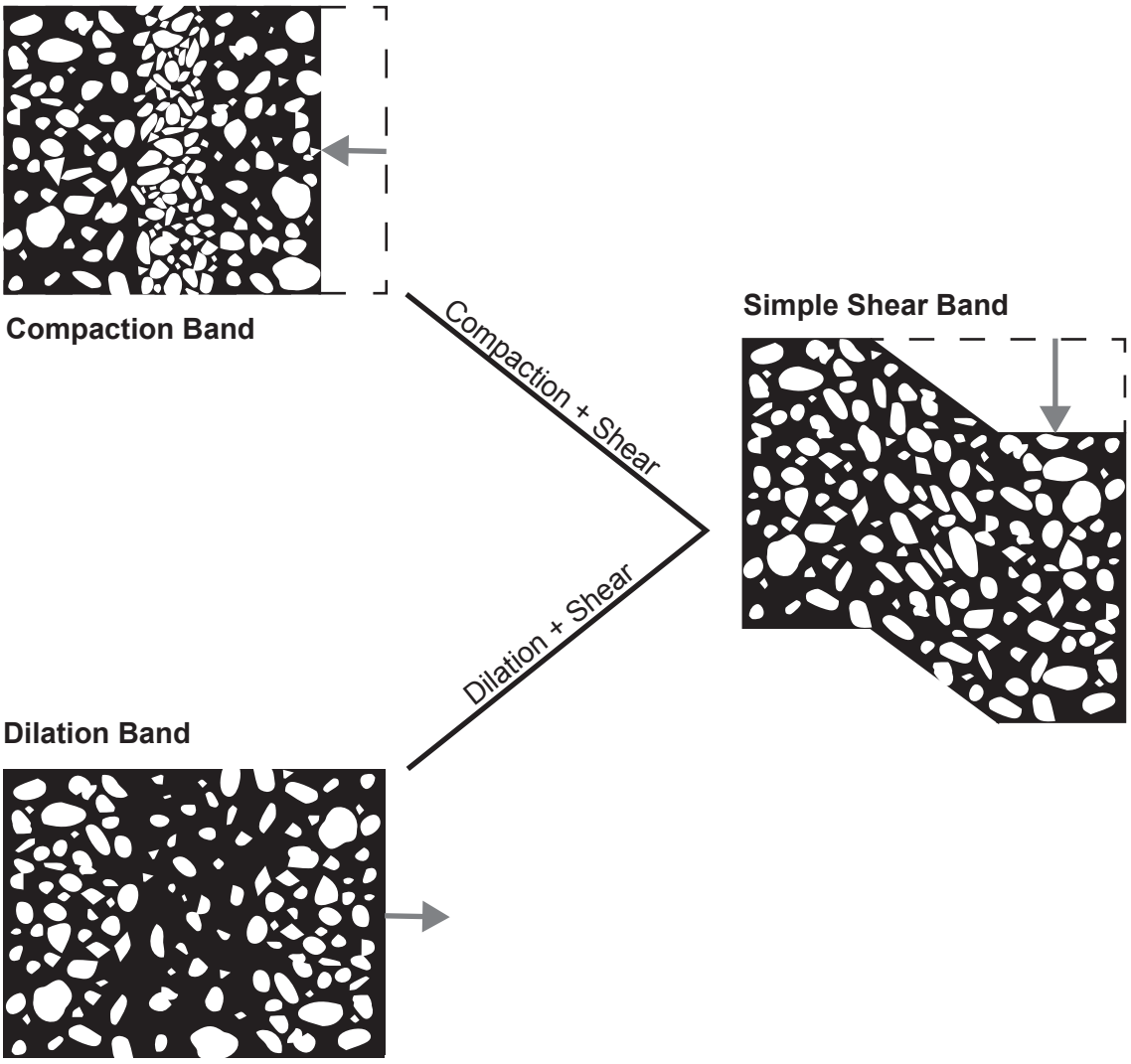

Figure 3. End-member deformation band styles of the kinematic classification scheme. Hybrid deformation bands combining either compaction and shear, or dilation and shear also possible. Modified from Fossen et al. (2007).

rocks, I will use deformation band in this paper to primarily refer to those that show compactional and/or shear behavior.

During deformation in porous rocks, inelastic yielding occurs first via strain hardening, during which deformation bands may localize, increasing the mechanical strength of the rock until strain softening failure can occur (Shultz and Siddharthan, 2005). This is in contrast with the behavior of crystalline rocks, which only exhibit strain softening behavior (by forming, e.g., joints, cracks, faults), because grain translation, rolling, and crushing will often collapse pore space and increase the internal cohesion of a rock (Schultz and Siddharthan, 2005). Deformation bands are a localized result of this strain hardening behavior. The occurrence of these tabular features in porous sandstones has implications for fluid flow in reservoir rocks because of their impact on permeability (e.g., Torabi and Fossen, 2009) and provides a tool for understanding tectonic deformation in a region (e.g., Jamison and Stearns, 1983; Eichhubl et al., 2010; Schultz, 2011; Ballas et al., 2014).

In deforming porous rocks, the directions of the principal stresses may be inferred from the orientations of deformation bands that form (e.g., Fossen et al., 2011; Klimczak et al., 2011). However, different kinematic classifications of deformation band will form at different angles with respect to the maximum compressive stress direction (σ_1). Pure compaction bands, for example, often form at high-angles to σ_1 (e.g., Mollema and Antonellini, 1996; Eichhubl et al., 2010). Deformation bands with a shear component will form more moderate angles with σ_1, often in conjugate sets (e.g., Klimczak et al., 2011; Ballas et al., 2014). There does not appear to be any consistent geometric pattern of

deformation band formation among rock units from different studies, as these characteristics likely vary with petrophysical properties.

Deformation bands in central California

The Etchegoin Formation is composed of marine sediments deposited during the upper Miocene-lower Pliocene in the San Joaquin basin at the southwestern edge of the present-day Central Valley in California (Loomis, 1990). At the time of deposition, the San Joaquin basin contained an inland sea that became increasing isolated from the Pacific Ocean as a result of the uplift of the Temblor and Diablo ranges (Loomis, 1990). The sediments of the Etchegoin Formation, which reach thicknesses up to 1672 m, were sourced from both Sierran arc materials and other volcanics to the north and east, and uplifted Franciscan Assemblage material in the Coast Ranges to the west (Loomis, 1990).

After deposition, the Etchegoin Formation was folded in several large-scale structures including the Parkfield syncline, Sunflower Valley syncline, Kreyenhagen Hills homocline, and several domed anticlines at Kettleman Hills, which were the focus of the field work presented here (Fig. 1). While not all the structures have ages, the Kettleman Hills anticline is quite young, forming in the past 2-2.5 m.y. (Harding, 1976; Wentworth and Zoback, 1989). The folds more proximal to the San Andreas fault may be older, with folding initiating during the Pliocene closer to the San Andreas fault and propagating northeastward into the San Joaquin basin (Dickinson, 1966; Harding, 1976). Folding in this region is thought to be controlled primarily by blind thrust faults resulting in fault-propagation and fault-bend folds (Namson and Davis, 1988). The young ages of

these structures indicate that they formed after the San Andreas fault became active in the region.

Deformation bands occur in outcrops of Etchegoin Formation sandstones within these larger folded structures and appear most well-developed in blue sandstone beds. In the winters of 2014 and 2015, I measured deformation bands as part of a larger field project on which other students from Carleton College have worked—including Alice Newman, Lucy Livesay, Erin Young-Dahl, and Grace Pipes—led by Dr. Sarah Titus. In outcrop, deformation bands often stand in relief against the host rock, suggesting that they are compactional deformation bands with increased cohesion relative to the surrounding rock (Fig. 2; Fossen et al., 2007). There also appears to be a shear component to many of these deformation bands. Where shear offset is evident along deformation bands, it most commonly indicates normal motion. In the field sites northeast of Parkfield, CA, we observe the range of possible deformation band clustering—from individual bands, to clusters of 2-5 bands, to zones of bands tens of centimeters thick (Fig. 2). Field sites in the Parkfield syncline, ~1 km away from the San Andreas fault, exhibit the most numerous and well-developed deformation bands, with many cross-cutting zones (Fig. 2d).

I present deformation band directions from across the field area, along with interpretations of their geometric and spatial patterns. Combining data from field stations spread over several square kilometers in each large-scale structure reveals a distinct pattern of two sets of steeply-dipping conjugate sets of deformation bands (Fig. 4). At Parkfield, Sunflower Valley, and Kreyenhagen Hills, there is consistently a conjugate set of NE-SW striking deformation bands, and another N-S to NNW-SSE striking conjugate

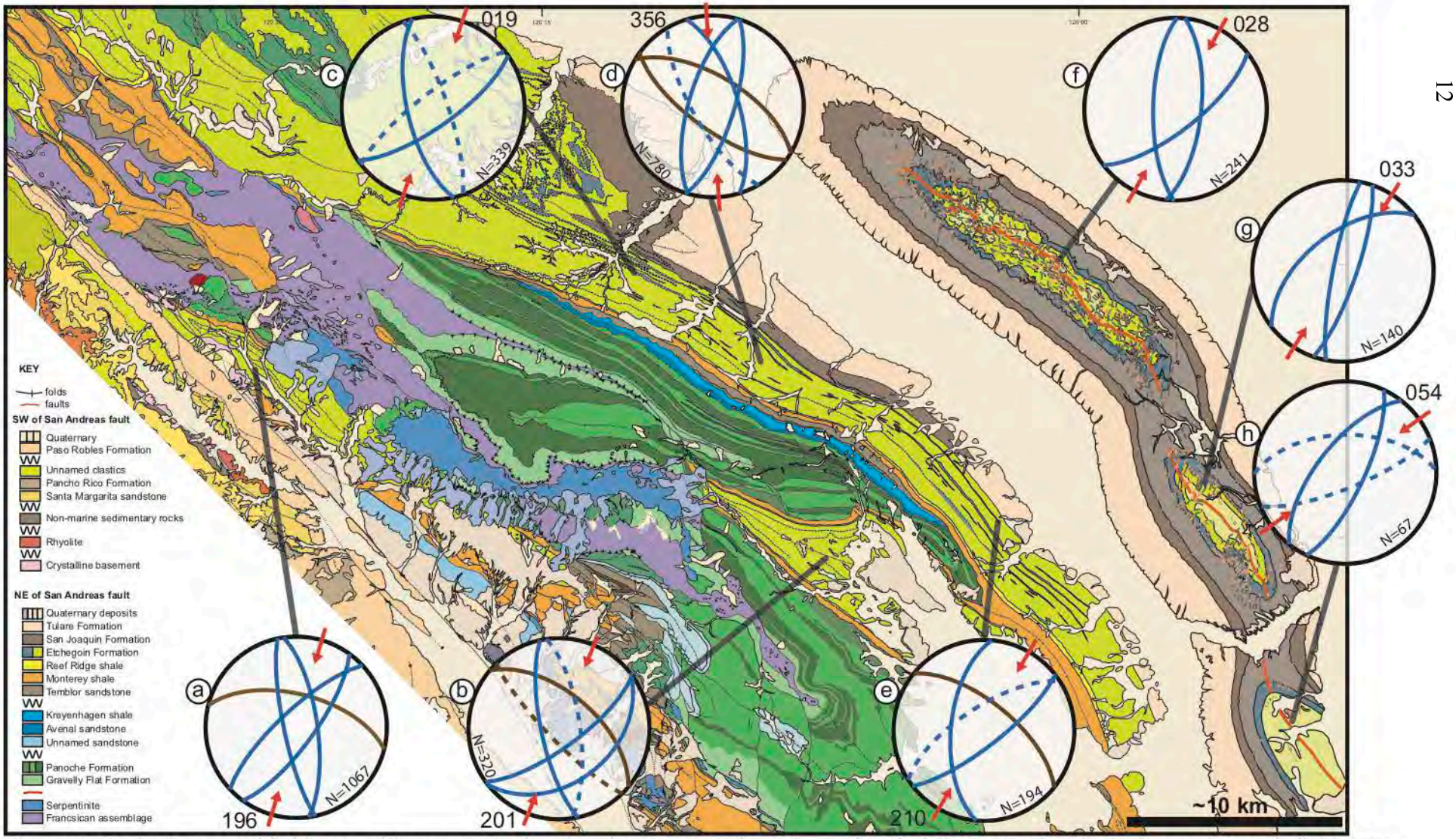

Figure 4. Geologic map of field area with stereonets showing the average orientations of each deformation band set observed at each field area: (a) Parkfield syncline, (b) Sunflower Valley syncline, (c) Kreyenhagen Hills North, (d) KH Middle, (e) KH South, (f) Kettleman Hills North Dome, (g) Middle Dome, (h) South Dome. Blue planes are part of the sets of conjugate sets that I use to infer S_{Hmax} (red arrows); brown planes represent the structure-parallel set. Map compiled from Woodring et al. (1940) for Kettleman Hills and Dibblee Foundation maps.

set. At Kettleman Hills, the data differ slightly from that of other field sites and vary between the North, Middle, and South domes. Particularly at North Dome, however, there is still a distinct pattern of conjugate sets. Sparse exposures of Etchegoin Formation sandstones at Middle and South Domes limit the quantity of data from these sites, although the average strikes of the measured deformation band sets exhibit a slight clockwise rotation relative to those of North Dome. Although members of each deformation band set are not visible at each individual field station, the aggregated data from a broader field area typically reveal similar deformation band orientations, resulting in the patterns shown in Figure 4.

There is another set of deformation bands often present that does not fit into this pattern of sets of conjugate sets. The strike of these deformation bands is often parallel to the local structural fabric. For example, at Kettleman Hills, there is a NW-SE striking set of moderately-dipping deformation bands that parallels the strike of the fold axis at North Dome (Fig. 4). This set of deformation bands is observed at most field areas, and may be associated with the folding of the large-scale structures, forming perpendicular to the local direction of maximum compressive stress.

Inferring the timing of deformation bands

To help constrain the timing of deformation band formation, I "unfold" the structures in which deformation bands were measured to determine the most likely timing of deformation bands development in the Etchegoin Formation as either: pre-, syn-, or post-folding. By rotating bedding in a field area back to horizontal, and then performing the same rotation or series of rotations on deformation band data, I can compare the

geometric patterns of unrotated and *in situ* datasets, looking for the most symmetric patterns in the data.

The unrotation process varies depending on the structure from which the data come. For example, data from Kreyenhagen Hills is simply rotated about bedding strike through the smallest angle required to return bedding to horizontal. At Sunflower Valley, a plunging syncline, I use a two-step process that involves first "unplunging" and then rotating the data about bedding strike (Fig. 5). The pattern of deformation band orientations appears more symmetrical in the *in situ* data when compared with unrotated data. In the Sunflower Valley data in particular, *in situ* deformation bands orientations are similar between both the north and south limbs of the fold, whereas the unrotated data are discordant across the limbs of the fold (Fig. 5). The more symmetrical *in situ* data suggest that sets of conjugate sets of deformation bands likely formed syn- to post-folding. This relationship does not provide any precise temporal constraints, however, because the timing of folding itself is not well constrained beyond Kettleman Hills. Similar unrotating methods were used on earlier data from Kettleman Hills to also infer those deformation bands as syn- or post-folding, indicating there that deformation bands are younger than 2.5 m.y. (Newman, 2011). The results of unrotating the data do support using *in situ* deformation band data to infer principal stress orientations, rather than the unrotated data, and demonstrate that deformation bands are relatively recent structures in this region, forming at most since the Pliocene.

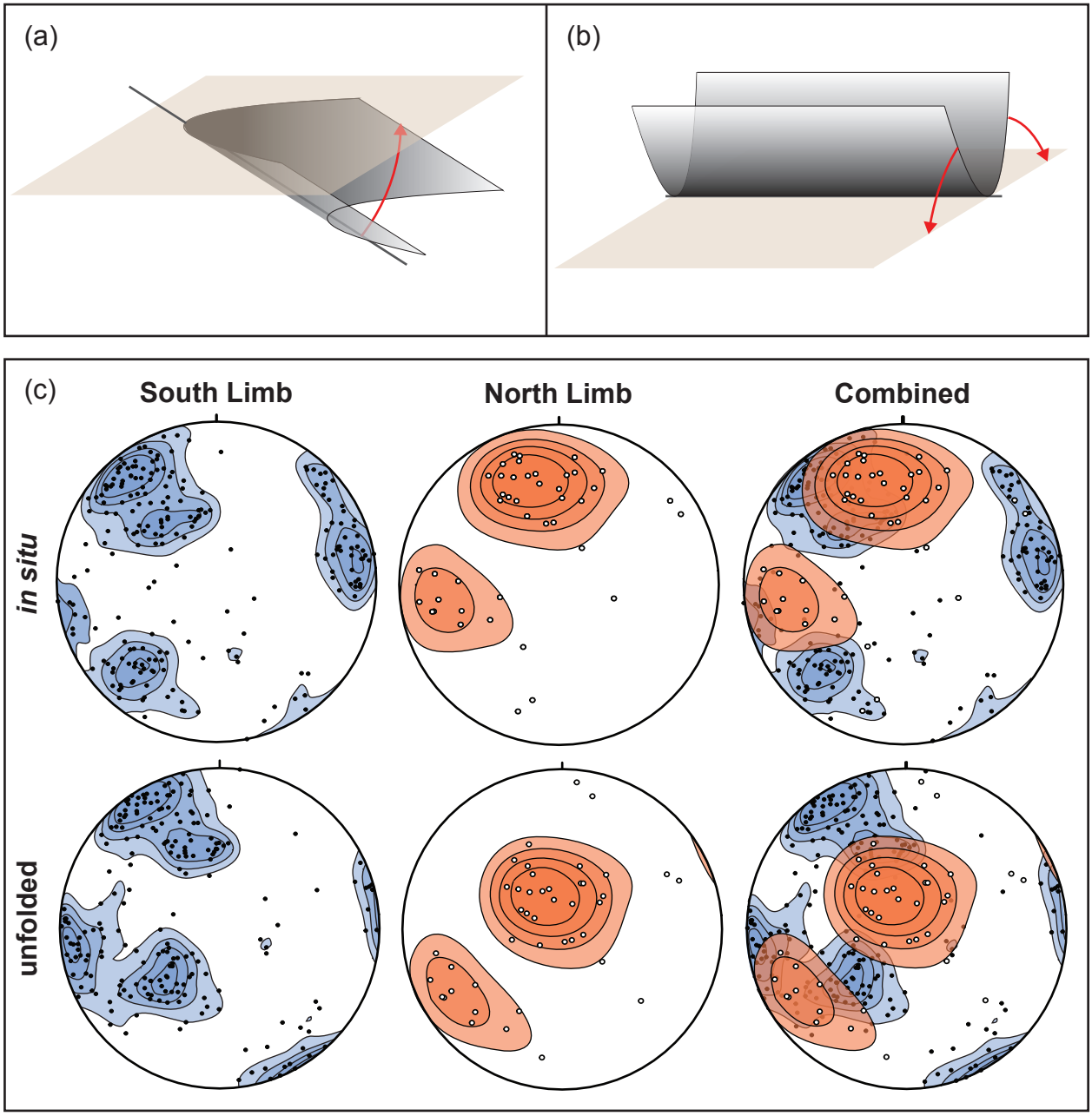

Figure 5. Schematic depicting the process of unrotating a fold to return bedding to horizontal by first (a) unplunging the fold and then (b) unfolding beds back to horizontal by rotating about bedding strike. If deformation bands formed prior to folding, applying the same rotations to *in situ* deformation band data should return them to their original direction. If deformation bands formed during or after folding, applying these transformations to the data may reduce the symmetry of patterns present in *in situ* data. (c) Stereonets with Kamb contoured data from each limb of the Sunflower Valley syncline comparing unfolded and *in situ* deformation band directions. Unfolded data exhibit reduced symmetry in comparison to *in situ* data, and the deformation band sets are most similar between the two fold limbs in the *in situ* data suggesting that deformation bands are syn- to post-folding developments in the Sunflower Valley region.

Inferring stress directions from deformation bands

I use the directions of deformation bands in the Etchegoin Formation to infer the direction of maximum horizontal compressive stress in the field area northeast of the San Andreas fault. To do so, I ignore the set of deformation bands that strike subparallel to the structural grain of the region and focus on the observed sets of conjugate sets. Because of their direction, I interpret the former group to reflect the direction of local stresses involved in folding, rather than that of regional stresses acting on the San Andreas fault. At Parkfield, crosscutting relationships with the latter set of deformation bands also support this interpretation, as members of the structure-parallel set are often offset by bands of the sets of conjugate sets, suggesting that the former developed earlier during deformation, perhaps more contemporaneous with folding.

Because of the sometimes crosscutting relationship of the sets of conjugate sets to the structure-parallel set of deformation bands, as well as the consistent pattern that is observed across the field area, I interpret these deformation bands as potential records of more regional stress directions. The pattern of sets of conjugate sets of deformation bands, as well as their observed, predominately normal, shear offsets, resembles the pattern of faulting in a three-dimensional stress field described by Reches (1983) (Fig. 6). Following this model, I inferred the direction of maximum horizontal compressive stress by calculating the direction of the small-angle bisector between the strike of the two sets (Fig. 4). This provided eight measurements of S_{Hmax} across the field area. The closest of these measurements to the San Andreas fault is within 2 km at Parkfield, CA, and the farthest is about 30 km to the northeast at Kettleman Hills. Measurements from the Kreyenhagen Hills region are split up into a north, middle, and south sections because of

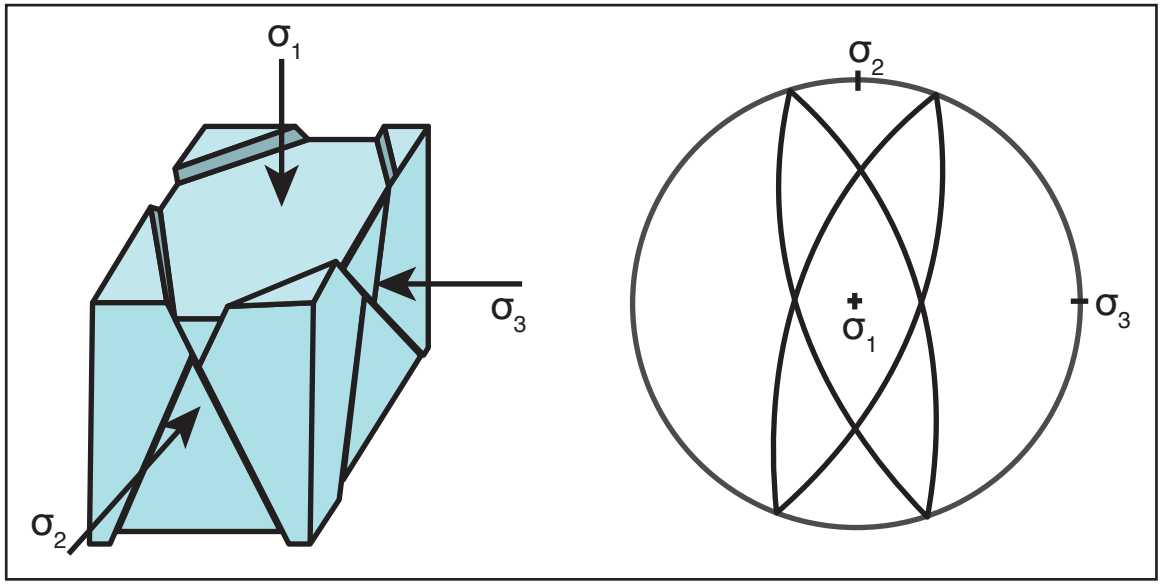

Figure 6. Block diagram depiction of the Reches model of faulting in a three-dimensional stress field. The resulting fault planes are plotted in the stereographic projection at right. In this case, σ_2 is the maximum horizontal compressive stress. In such a stress regime, S_{Hmax} can be inferred from the faults by taking the acute angle bisector between the strikes of the two sets of conjugate faults. Modified from Reches (1983).

the broad geographic distribution of field sites there. Deformation band data yield values for S_{Hmax} that are directed between 356° and 054°, but most commonly at 020° to 030° (Fig. 4). These directions are 60° to 70° to the strike of the San Andreas fault in this region (~320°) (Fig. 1).

The intermediate angles of S_{Hmax} with the San Andreas fault as inferred from deformation bands stand in contrast with the high angles reported by the World Stress Map. To assess the validity of the deformation band-derived S_{Hmax} interpretations and their value as a check on other S_{Hmax} measurements, it is necessary to better understand how deformation bands form in the Etchegoin Formation. Are the conjugate sets of conjugate sets that are observed in central California true records of regional stresses, and is the Reches faulting model an appropriate tool for interpreting these data? The experiments presented here are an attempt to answer the question of how deformation bands form in the Etchegoin Formation by deforming sandstone samples under controlled stress conditions in the laboratory.

TRIAXIAL DEFORMATION EXPERIMENTS

Deformation bands in previous triaxial experiments

Triaxial deformation experiments are a common tool for assessing the mechanical properties of rocks and for further exploring deformation structures observed in the field (e.g., Handin et al., 1953; Handin and Hager, 1963; Cilona et al., 2012; Wong and Baud, 2012). These experiments provide a means of simulating stress conditions found in the Earth's crust, which allows researchers to deform rocks in a controlled setting, thereby providing insight into the deformation history of naturally deformed rocks. Triaxial

experiments commonly involve a chamber in which a sample is subjected to a confining pressure to simulate the weight of overlying rock and often a differential stress to simulate, for example, some additional tectonic stress (Fig. 7a).

Previous triaxial deformation studies on a variety of sandstones, and even some carbonates, have successfully produced deformation bands under laboratory conditions (e.g., Mair et al., 2000; Tembe et al., 2008; Cilona et al., 2012). The type of deformation bands that form is controlled by several factors, including host rock porosity, grain packing and sorting, the presence of pore fluids, confining pressure, differential stress, and the stress path of a rock from an undeformed state to inelastic yielding (Schultz and Siddharthan, 2005; Cheung et al., 2012). As a result, contrasting types of deformations bands may form in the same rock under different stress conditions and in different rocks under the same stress conditions.

Theoretical and experimental methods have demonstrated that, generally, the magnitude of stresses required to initiate inelastic deformation, and therefore deformation band formation, in a porous rock decreases with increasing porosity and grain size (Schultz and Siddharthan, 2005). Sandstones with relatively uniform grain size distributions also tend to be more prone to developing compaction bands than those with broad grain size distributions, likely because of the micromechanical processes behind grain crushing (Cheung et al., 2012). The presence of feldspars and lithic grains in a sandstone will also tend to lower the yield strength of a rock, and therefore the point at which certain structures localize, perhaps influencing the types of structures that are likely to form in a specific rock unit (Fossen et al., 2011). At high enough mean stresses ($(\sigma_1 + \sigma_2 + \sigma_3)/3$), porous rocks will deform via distributed cataclastic flow rather than via

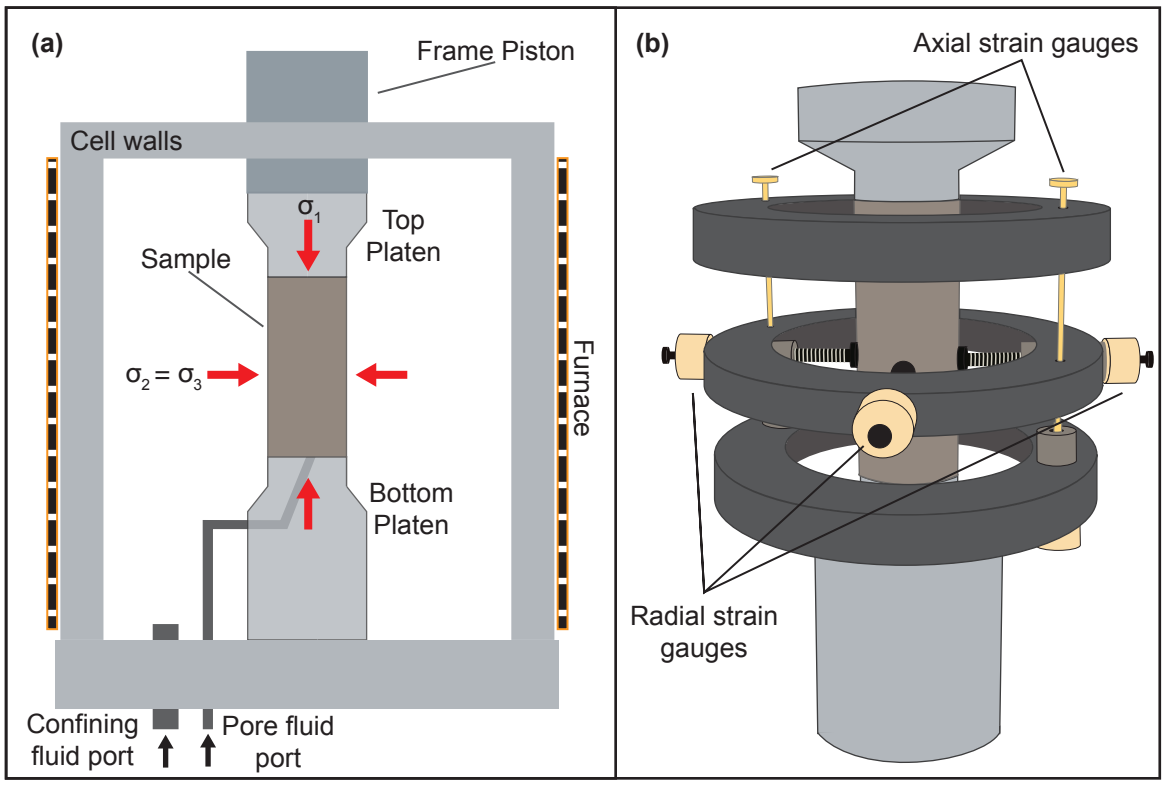

Figure 7. Schematics of triaxial deformation experiment setup in the RTR 2000 testing rig: (a) cross section through the pressure vessel that is filled with confining oil during experiments, and (b) strain gauge arrangement with two axial strain gauges and four radial gauges arround the sample, housed in rings that attach to the sample with screws (not shown). The sample is affixed to the platens with a plastic heat-shrink wrap.

the formation of localized structures like deformation bands (Wong and Baud, 2012). When considering all of these controls on the deformation style in concert, it is apparent that the stress conditions at which certain structures develop will vary significantly between different lithologies.

Experimental studies focused on deformation band formation often explore the impact of varying the effective confining pressure and the amount of axial strain applied to samples between separate experimental runs on the same rock type. Compactional deformation bands are the most common focus of experiments – including both pure compaction bands and shear compaction bands – and fewer studies have been conducted producing dilation bands (e.g., Bésuelle et al., 2000; Alikarami and Torabi, 2015). Suites of deformation experiments often reveal changes in deformation band type, orientation, and maturity. For example, increasing confining pressure can cause a shift from deformation via conjugate shear bands to pure compaction bands, and increasing axial strain may prompt the development of additional deformation bands or more well-developed deformation bands (Baud et al., 2004; Tembe et al., 2008). Deformation band formation in general, however, is primarily observed under stress conditions in the transitional zone between the brittle faulting regime to the distributed cataclastic (or "ductile") flow regime (Wong and Baud, 2012).

In studies that successfully produce deformation bands in triaxial experiments, the bands appear to take several forms. For example, Mair et al. (2000) report mm-wide zones of shear and compaction localization that are visible on the exterior of samples as light-colored zones. Baud et al. (2004) observe finer structures that they classify as diffuse and discrete compaction bands. Discrete bands are characterized as deformation

bands less than or equal to ~3 grain diameters in thickness and accommodate strain by developing sets of sub-parallel arrays oriented perpendicular to σ_1. These deformation bands appear macroscopically as fine, dark zones of grain crushing visible in thin section. Diffuse bands, including higher-angle shear bands, are thicker than discrete bands and accommodate strain via lateral propagation and may develop in conjugate sets. These diffuse bands are likely similar to those shear bands observed by Mair et al. (2000). Although some sandstones observed develop only one kind of these deformation bands, some samples exhibit both styles of deformation localization (Baud et al., 2004). Other authors of triaxial studies report deformation bands that appear either similar to those of Mair et al. (2000) or Baud et al. (2004), or somewhere in between these two styles (e.g., Bésuelle et al., 2000; Wong et al., 2001; Tembe et al., 2008). Those deformation bands produced by Mair et al. (2000) appear the most similar to those observed in the field.

Such previous triaxial deformation studies characterize deformation in sandstones using mechanical data obtained during experiments, as well as post-test analysis of samples in thin section. Following the same general procedure, I attempted to generate and characterize experimental deformation bands in the Etchegoin Formation sandstone to compare with those we observe in central California.

Triaxial experiments on Etchegoin Formation sandstone

Samples of the Etchegoin Formation sandstone that I used in the laboratory experiments were collected at Kettleman Hills, approximately 30 km northeast of the San Andreas fault. The specific Etchegoin sandstone sample used in these experiments is fine-grained and has an average porosity of 41.5%. These poorly consolidated samples

are composed predominately of grains of plagioclase feldspar and quartz, and contain notable quantities of lithic grains, as well as trace amounts of micas, amphiboles, and other minerals.

Sample processing and triaxial deformation experiments were performed in the lab of Dr. Melodie French at Rice University. Six cores, 25 mm in diameter and ~50 mm long, were taken from one hand sample. Bedding in three of the cores is oriented parallel to the long-axis of the core and is perpendicular in the other three. The cores were jacketed with a plastic heat-shrink wrap and bathed in warm water to flush out salts that had precipitated in the pore space. Before beginning triaxial tests, samples were saturated with water under vacuum for at least three hours.

When setting up a triaxial deformation experiment, I affixed cores to platens using more plastic heat-shrink wrap and attached strain gauges around the outside of the core (Fig. 7b). Four gauges affixed around the circumference of the core monitored radial strain in the sample, while two gauges mounted in rings affixed to the top and bottom of the core recorded axial strain.

The RTR-2000 Rapid Triaxial Rock Testing System from GCTS, into which the samples are placed, is a triaxial deformation rig with hydraulically controlled confining pressure, pore fluid pressure, and axial load systems (Fig. 7a). The confining fluid system uses a silicon oil that fills the vessel containing the jacketed core and can be pressurized up to 140 MPa. This system maintains a pore fluid pressure within the samples using water, and pore volume change within cores may be monitored during experiments by measuring the change in the water volume in the system. The difference between the confining pressure and the pore fluid pressure is the effective confining pressure, P_{eff},

which in these experiments is equal to both the intermediate and minimum compressive stresses (σ_2 and σ_3, respectively). A furnace surrounding the entire vessel allows heating of the unit up to 200°C, and internal temperature can be maintained to within ±0.5°C.

An axial load piston contacts the top platen above the core and applies a force to the sample, which is the maximum compressive stress, σ_1. A pressure transducer attached to the piston within the vessel measures the differential stress on the core. For the experiments here, the piston was programmed to advance at a constant rate, deforming the sample at a roughly constant axial strain rate. Strain rates varied between experiments from 10^{-7} s^{-1} to 10^{-6} s^{-1}. Confining and pore fluid pressures, as well as temperature, were maintained at constant values during the experiments, thereby simulating conditions in the crust at about 1 km depth. Refer to Table 1 for details on the experimental conditions in each test.

The suite of experiments was conducted with the axial stress oriented parallel and perpendicular to bedding within the cores and at axial strains between 2% and 10% to examine the impact of these variables on deformation in the Etchegoin sandstone. Within each of the bedding-parallel and bedding-perpendicular sets of cores, samples were deformed to axial strains of 2-5%, 7-8%, and 10%. The samples also experienced small amounts of axial and radial strain prior to the start of experiments while loading the confining and pore pressures.

After each experiment, the deformed core was dried in an oven to remove water from the pore space before being vacuum impregnated with blue-dyed epoxy. Epoxied samples were cut longitudinally down the middle of the core, perpendicular to the expected strike of any potential deformation bands, as noted visually or inferred from

Sample ID	Bedding Orientation	Confining Pressure (MPa)	Pore Pressure (MPa)	Max σ_d (MPa)	Prescribed ε_a (%)	Total ε_a (%)	Strain Rate (s^{-1})
KH8b-1	perpendicular	40	20	6.74	2.03	6.70	1.50×10^{-7}
KH8b-3	perpendicular	10	5	10.36	9.82	10.2	3.01×10^{-6}
KH8b-4	perpendicular	10	5	7.78	6.11	6.56	2.94×10^{-6}
KH8b-6	parallel	10	5	10.22	8.92	9.30	3.09×10^{-7}
KH8b-7	parallel	10	5	9.62	6.27	7.90	3.00×10^{-7}
KH8b-8	parallel	10	5	11.15	4.45	~ 9.4	1.07×10^{-6}

Table 1: Bedding orientation is given relative to the long-axis of the cylindrical samples. Prescribed ε_a is the axial strain accommodated during tests, while total ε_a includes axial strain accommodated by the samples during loading of confining and pore pressures prior to tests. All experiments were conducted at $\sim 47\,^{\circ}$C. For sample KH8b-8, $\sim 5\%$ axial strain was inadvertently applied by rapid advancement of the axial piston into the sample prior to loading confining and pore pressures.

anisotropic radial strain data, and thin sections were made from four deformed samples and one undeformed samples. Because of the incompetence of the Etchegoin Formation sandstone that was used, post-test sample processing was difficult and several samples disaggregated before thin sections could be made.

Experimental Results

Mechanical data

The strain gauges attached to each sample record data that provide insight into the behavior of the Etchegoin Formation sandstone during deformation. Plots of differential stress, volume strain, and axial strain help characterize the deformation that occurs during an experiment (Fig. 8). In these plots, I use the convention for reporting strain in which positive values indicate compaction and negative values indicate dilation.

Several consistent patterns emerge from these experiments. All cores exhibited continuous strain-hardening behavior as illustrated on the stress-strain curves. This behavior can be seen in how the slope of the stress-strain curve decreases but remains positive after initial axial loading, indicative of inelastic yielding (for experiments conducted to axial strains greater than 5%). The shape of stress-strain curves is fairly similar for all samples and there is little significant difference in strength between samples with axial strain oriented parallel and perpendicular to bedding. There does not appear to be an appreciable difference between the stress-strain curves of samples in which bedding was oriented parallel to axial strain and those in which it was perpendicular. On inspection, the stress-strain curves of samples subjected to similar magnitudes of axial strain have similar shapes regardless of bedding direction in the

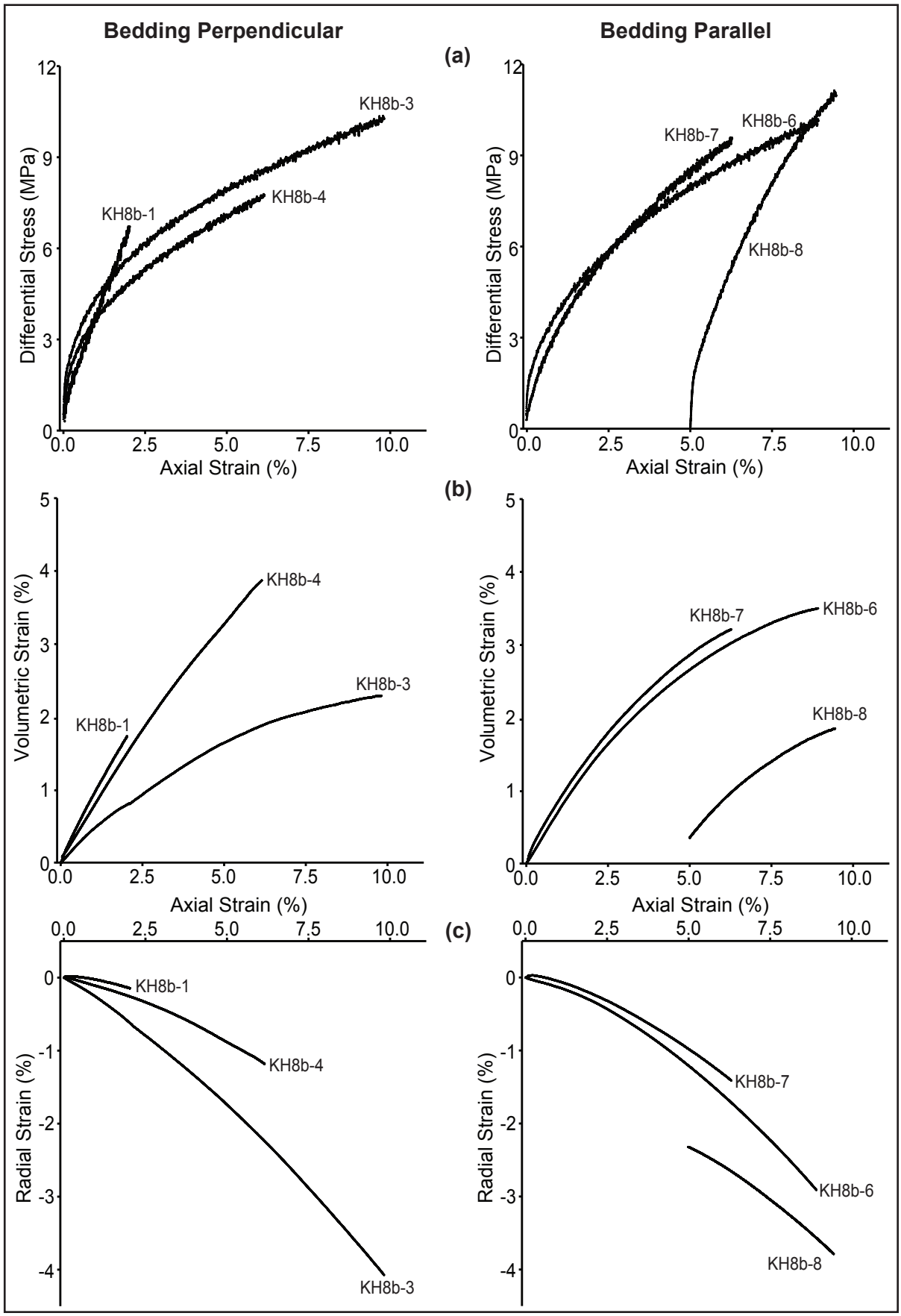

Figure 8. Plots of mechanical data gathered during triaxial experiments for samples with axially perpendicular and axially parallel bedding. (a) differential stress, (b) volumetric strain, and (c) radial strain versus axial strain.

sample. Radial and volumetric strains also behave similarly between experiments (Fig. 8bc). The most significant difference is in the magnitudes of radial and volumetric strains, which are lower for samples subjected to lower axial strains than for those subjected to greater axial strains.

Despite accumulating up to 10% axial strain, samples only accommodated differential stresses up to ~11 MPa (Table 1). This indicates that Etchegoin Formation sandstone is a fairly weak material—i.e., the samples compact easily and cannot accommodate high differential stress without accumulating relatively large amounts of strain.

Thin sections from deformed samples

Deformed cores of Etchegoin Formation sandstone did not contain any obvious deformation bands, nor any other strain-localization feature, on visual inspection after each test. I later confirmed this initial observation by analyzing thin sections of deformed samples with both optical and scanning electron microscopy. Analysis of these samples nonetheless allows qualitative observations of grain-scale deformation. Further, I analyze samples using ImageJ image processing software, to quantify some grain-scale deformation characteristics of the Etchegoin Formation sandstone (Rasband, 2016).

Qualitative investigation of thin sections and backscattered electron (BSE) images of the samples used here reveals several apparent differences between undeformed and experimentally deformed Etchegoin Formation samples (Fig. 9). Most significantly, deformed samples appear to exhibit reduced porosity and greater fracture density in comparison to undeformed samples. Curiously, fractures that are oriented perpendicular

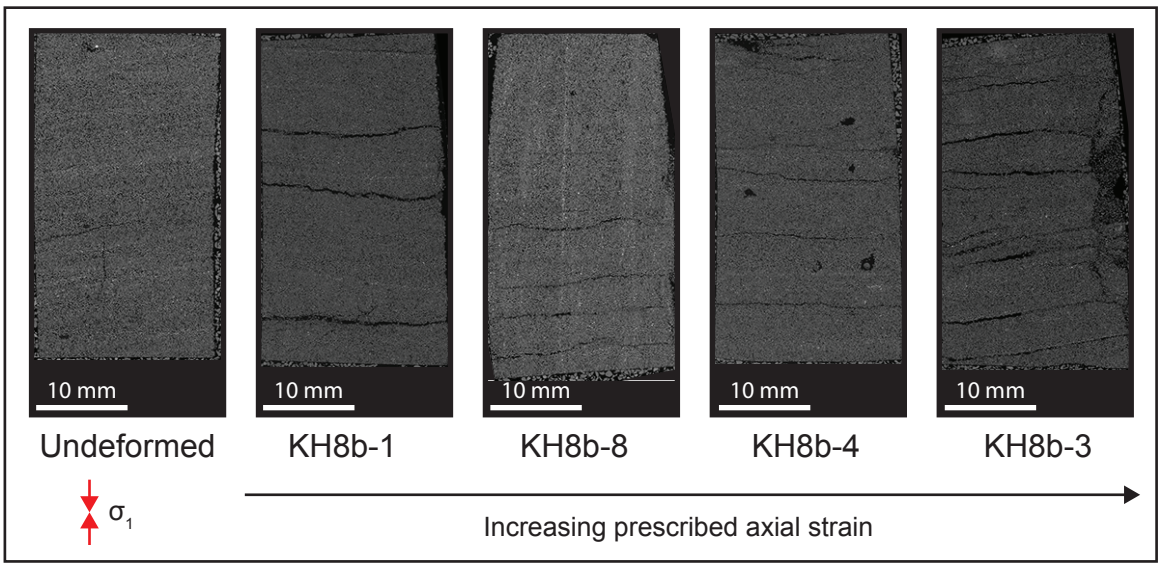

Figure 9. BSE images of thin sections from undeformed and deformed samples taken at 45x magnification. Deformed samples are arranged in order of increasing axial strain applied during experiments. All samples but KH8b-8 have axially-perpendicular bedding. Missing material from the edge of samples – particularly from KH8b-3 – is a result of post-testsample processing. Not all samples are presented here because some were lost during processing.

to the applied σ_1 and extend nearly the diameter of the samples are also apparent in thin section.

While grain damage is not widespread in the undeformed sandstone sample, fractured grains are visible throughout deformed samples. Following the classification scheme of Chuhan et al. (2002), grain damage in deformed samples ranges from grain flaking, where fractures occur along grain margins, and single fractures, where a grain is split in two, to irregular complex fractures and grain crushing (Fig. 10). Grain flaking and irregular complex fractures are the predominant fracture type, and grain crushing is rarer. The amount of grain damage in the samples at first appears to have a positive correlation with the amount of axial strain applied to the sample. Naturally deformed samples of the Etchegoin Formation hosting deformation bands appear even more deformed than experimental samples. Grain damage is more extensive in the field samples and grain crushing more prevalent, even in the host rock of the deformation bands.

Porosity. To estimate the porosity of sample prior to the experiments, I use a saturation method. In this method, porosity is calculated by dividing the mass difference between a dry sample and a sample saturated with water under vacuum for several hours by the volume of the cylindrical sample. The porosity of each undeformed core was calculated using this method before each experiment. The average initial porosity of the samples used in the experiments presented here was 41.5%.

Because of the delicate nature of specimens after the experiments, I estimate the pore area (in 2D rather than 3D) from thin sections. In the process of removing samples from the testing rig, some material is often lost, and saturating cores with water would further

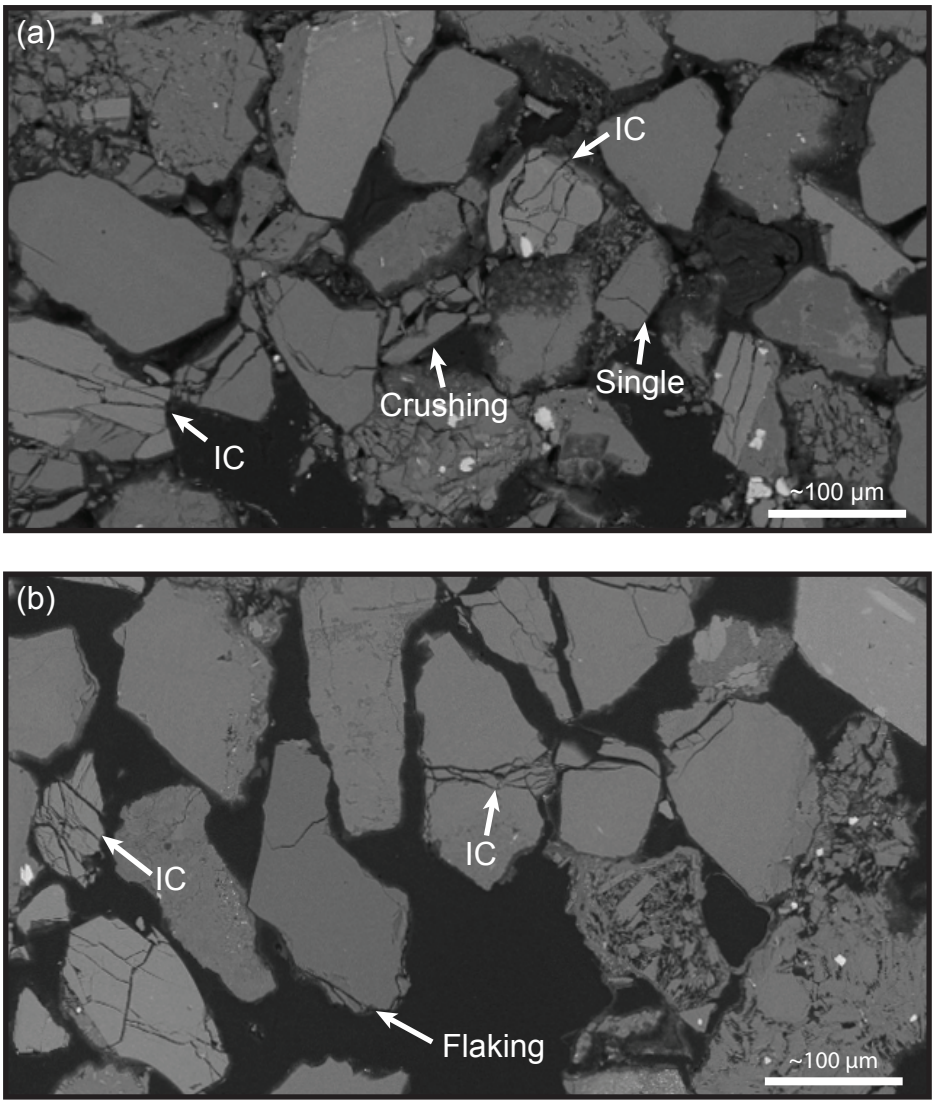

Figure 10. Examples of types of grain damage common in deformed samples: single fractures, irregular complex fractures (IC), grain flaking, and grain crushing in (a) KH8b-1 and (b) KH8b-4.

compromise their post-test condition. Note that in approximating porosity from a single thin section of the samples, I assume that pore volume strain accommodated during triaxial loading was homogeneous in the sample. An image of each thin section was produced with the back-scatter electron (BSE) detector on the Hitachi S-3000N Scanning Electron Microscope at Carleton College. Images from BSE scans were analyzed with ImageJ software to determine post-experiment porosity. For each thin section, I selected multiple sub-sections from which to measure porosity, focusing on regions between the open fractures. Manual greyscale thresholding methods were used to highlight the pore space in these cropped images, which enabled measurement of the area fraction occupied by pore space. Because of the subjectivity of manual thresholding, I took pore area measurements representing what appeared to be the minimum and maximum possible threshold values, providing a measure of uncertainty.

Measurements of porosity in the undeformed sample taken using ImageJ do not correspond exactly to those from saturation measurements. Threshold measurements of the BSE scan of an undeformed sample indicate a porosity of 36.5% ± 0.7%, compared to the average 41.5% initial porosity measured prior to experiments. Because of this discrepancy, I focus on the relative differences in image-derived porosity between samples (Fig. 11). Despite different experimental conditions, porosity is fairly similar among the deformed samples. Relative to the porosity of an undeformed sample determined from BSE images, post-test measurements indicate porosity reductions ranging from 7% to 14%. Although the associated uncertainties of these measurements suggest that the true porosity values may all be fairly similar, sample KH8b-3, which experienced the most axial strain, exhibits the greatest porosity reduction (Fig. 11). The

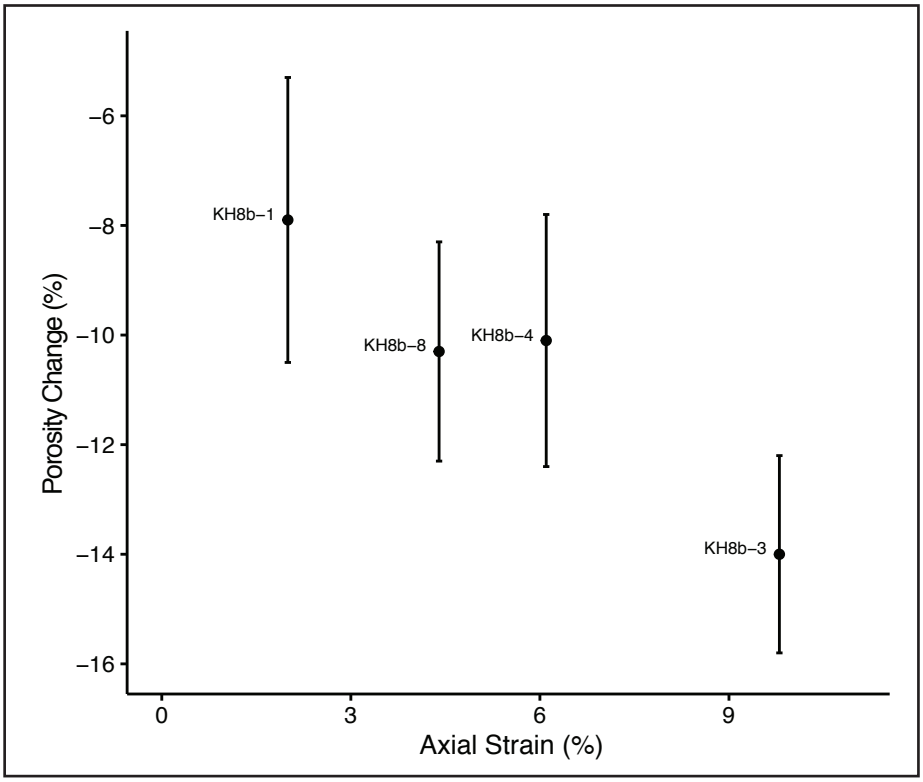

Figure 11. Pore area change in deformed samples relative to the pore area of the undeformed sample measured with ImageJ. These data suggest that pore space decreases as samples accommodate more axial strain, although volumetric strain data gathered during experiments do not suggest such a correlation and instead show that total volumetric strain is comparable across all samples (Table 2).

Sample ID	Pre-test ε_v %	During-test ε_v %	Total ε_v %
KH8b-1	8.77	1.74	10.51
KH8b-3	0.94	2.32	3.26
KH8b-4	0.59	3.85	4.44
KH8b-6	1.20	3.55	4.75
KH8b-7	1.52	3.31	4.83
KH8b-8	0.36	1.77	2.13

Table 2: Volumetric strain as measured by the strain gauges attached to samples in the testing rig. Pre-test strain results from loading confining pressure, while volumetric strain accommodated during tests is primarily from axial compression. Total strain takes both of these into account.

porosity measurements from image analyses seem to be at odds with mechanical measurements of volume strain during experiments and loading (Table 2). Volume strain data calculated from the strain gauges would suggest that KH8b-1 should have experienced the greatest porosity decrease because of the large amount of volume strain accommodated by the sample while the confining and pore pressures were loaded. However, there is little correlation between the strain gauge data and image analysis data.

I used the same ImageJ porosity analysis technique on a sample from Kettleman Hills hosting several natural deformation bands. Porosity in the host rock within ~1 cm of deformation bands is comparable to that of the deformed samples and is most similar to that measured in sample KH8b-1. Porosity in the deformation bands is reduced by 24.3% ± 3.9% relative to the surrounding host rock.

Grain damage. All samples, including the undeformed sample, exhibit grain-scale fracturing. Fractures provide some indication of the micromechanisms of deformation and how deformation in the sample is accommodated at the grain scale. Many irregular complex fractures within grains are Hertzian in nature, in that they emanate from contacts with surrounding grains and likely initiate from contact loading at grain boundaries (Zhang et al., 1990).

In 100x magnification BSE image transects, taken parallel to the direction of σ_1 along the length of each thin section, I used Adobe Illustrator to trace distinct, single, irregular complex, and flaking intragranular fractures (Fig. 12). Particle analysis in ImageJ fit an ellipse to each fracture trace and provided the direction of the major axis of each ellipse, as well as the location of each ellipse in the image. Histograms of the

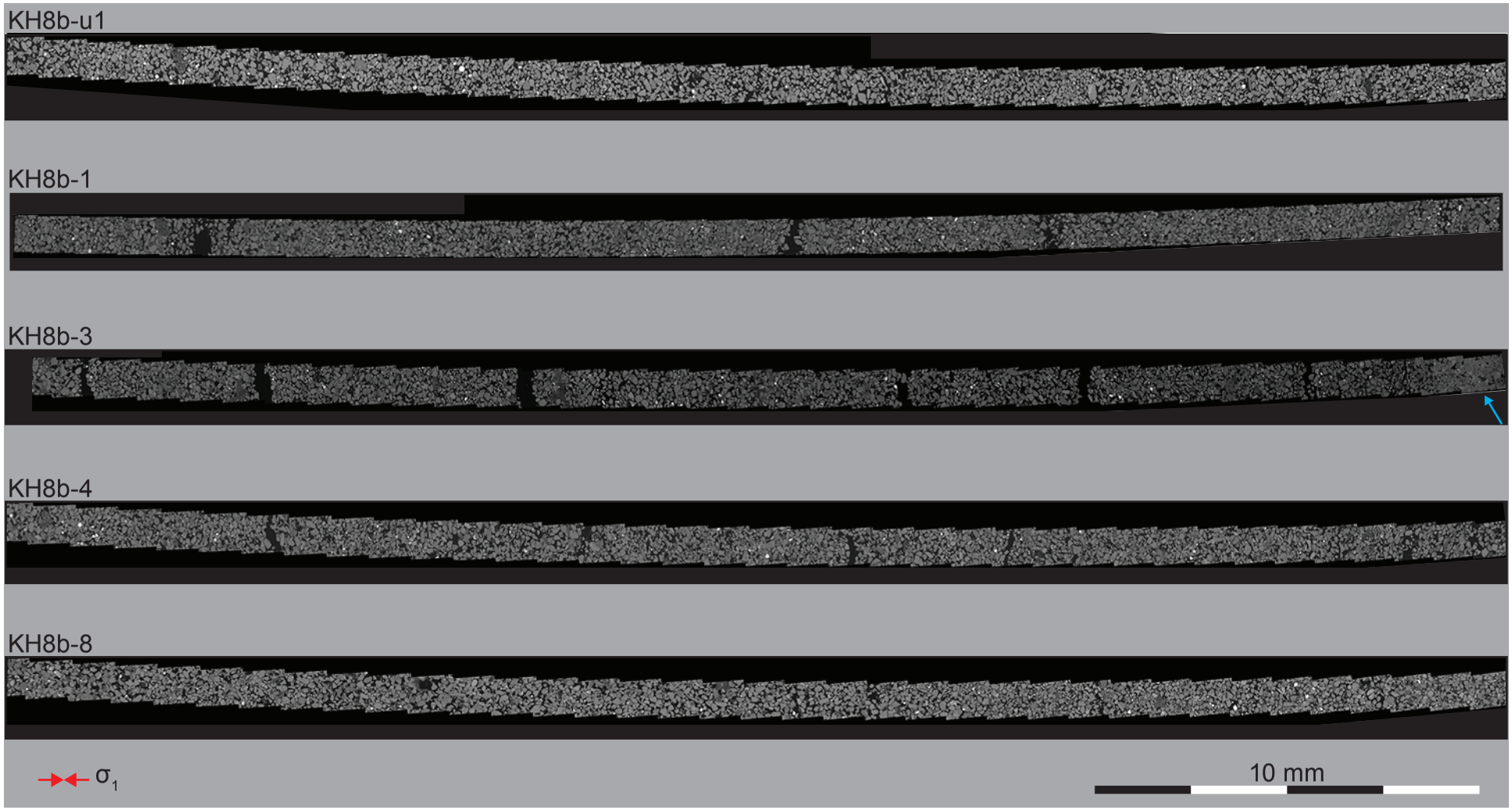

Figure 12. 100x magnification BSE image transects across each sample. Fractures across each transect were traced in Adobe Illustrator and these traces were analyzed in ImageJ to measure fracture direction (Fig 15). The blue arrow points to the area in the KH8b-3 that has abnormally high amounts of calcite cement.

distribution of these fractures across the transects provide some indication of the distribution of grain fracturing in the sample (Fig. 13), and rose diagrams show the direction of all the fractures measured in each transect (Fig. 14).

Most deformed samples exhibit similar fracture densities and have fracture counts about twice as high as that of the undeformed sample. The histograms and counts of fractures in the transects do not reflect the amount of grain crushing present, because I did not trace fractures in crushed grains due to the complexity of their fracture networks. I instead made qualitative descriptions of the relative amounts of grain crushing in each transect. There is little to no grain crushing present in the undeformed sample, while the most widespread grain crushing appears in sample KH8b-1, which experienced the highest effective confining pressure. The other deformed samples exhibit similar amounts of grain crushing, with the highest apparent density in KH8b-3, and lowest in KH8b-4. The difference in grain crushing density between these samples is not clearly pronounced, however, and grain crushing density seems to reflect the total fracture density.

Grain-scale fracturing is not distributed homogeneously across the transects, nor does it show any strong preferential localization within the samples. Note, however, the anomalously high fracture density near one end of KH8b-8 (Fig. 13). This is likely related to the high differential stress mistakenly applied to the sample by the axial piston prior to loading confining and pore pressures. Conversely, there is a relatively low fracture density at one end of sample KH8b-3 that correlates with an anomalously well-cemented region of the sample (Fig. 12). The calcite cement in this part of the sample likely cushioned grains during deformation, as has been observed in other experiments

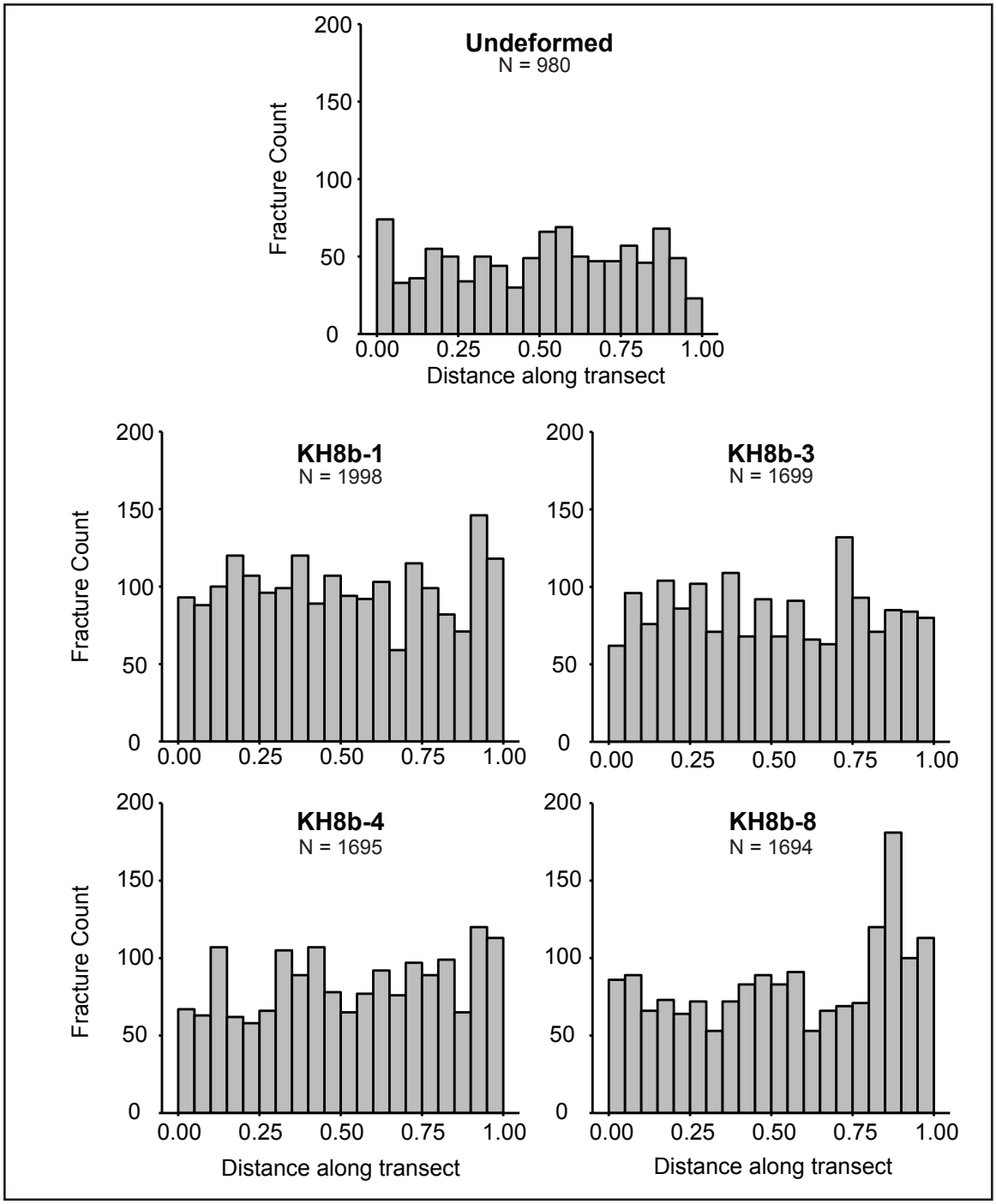

Figure 13. Histograms of fracture counts along each transect. Note the relatively uniform distribution of fractures across transects. Distance along transect is normalized by the length of the transect (~39 mm).

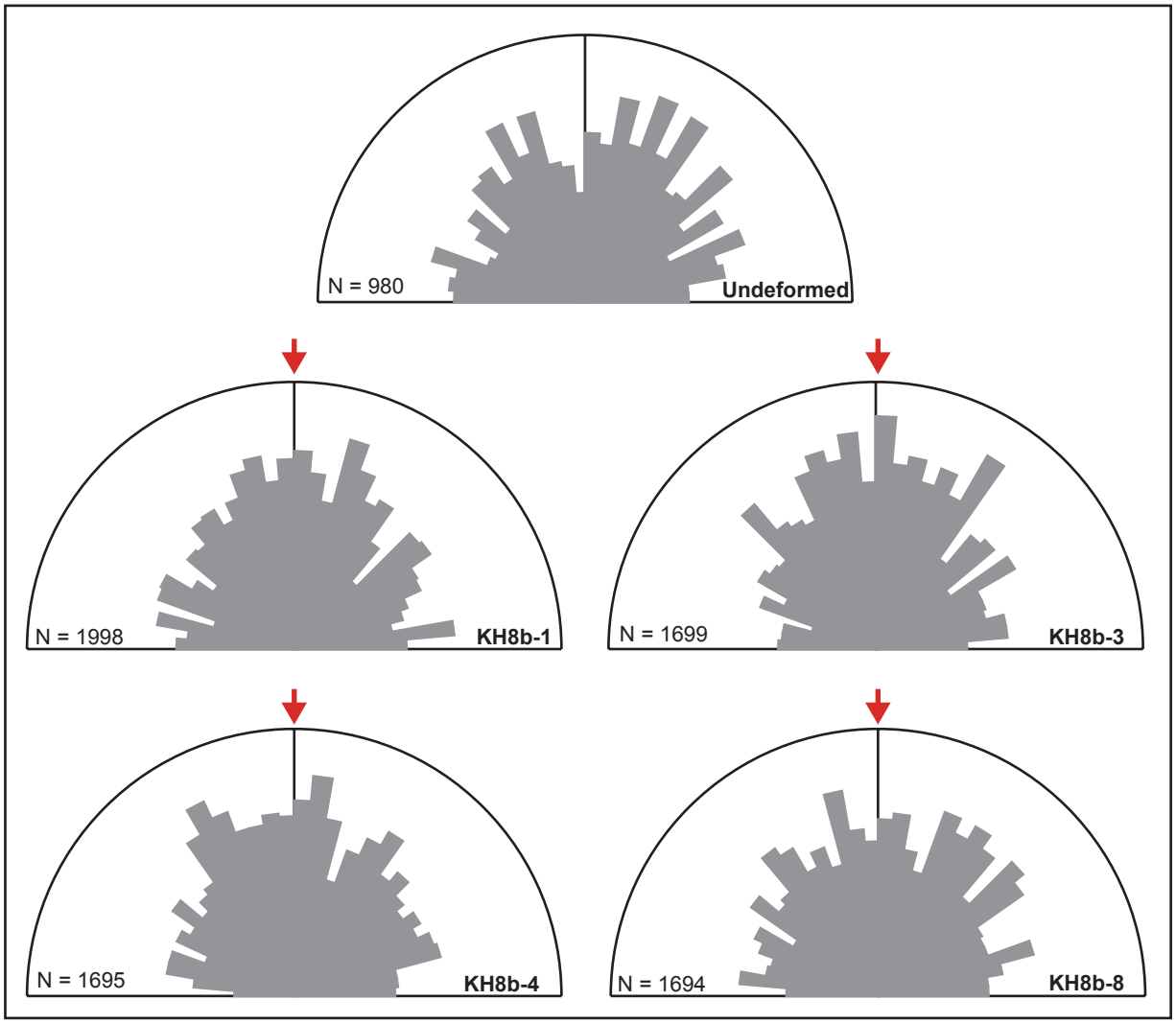

Figure 14. Rose diagrams showing the direction of fractures measured along each transect of the deformed samples. Red arrows indicate the direction of σ_1. Bars extended to the radius of the circle represent bins containing 5% of the data of the whole set. There is no apparent significantly preferred direction of fractures in the deformed samples.

(Menéndez et al., 1996). This could explain the low fracture density in this part of KH8b-3 relative to the rest of the mostly cement-poor sample. Elsewhere along the sample transects, fracture density varies somewhat, perhaps reflecting the development of isolated zones of Hertzian fracturing.

The directions of fractures throughout the transects display a slight preferred orientation subparallel to the axis of the sample (i.e., subparallel to σ_1) in some of the samples (Fig. 14). However, there is a large amount of variability in the data, and the fractures in sample KH8b-8 do not exhibit a strongly preferred direction. Fracture directions also do not vary significantly over the length of the transect (Fig. 15). A closer analysis of the directions of these fractures, perhaps using spatial statistics to quantify the differences between samples, would provide an improved understanding of changes in grain-scale deformation between samples. It is important to note that fracture direction data are collected from two-dimensional slices through the cylindrical samples, and therefore may not reflect the true direction of granular fractures in the samples.

DISCUSSION

Implications of experimental results and comparison with other triaxial studies

Although the triaxial tests conducted in this study failed to produce deformation bands in the samples – perhaps indicating the conditions at which deformation bands likely do not form in the Etchegoin Formation sandstone – these experiments have provided useful information on how the Etchegoin Formation behaves during deformation. For the relatively fine-grained samples studied here, mechanical data collected during triaxial tests suggest that the direction of bedding relative to σ_1 has little

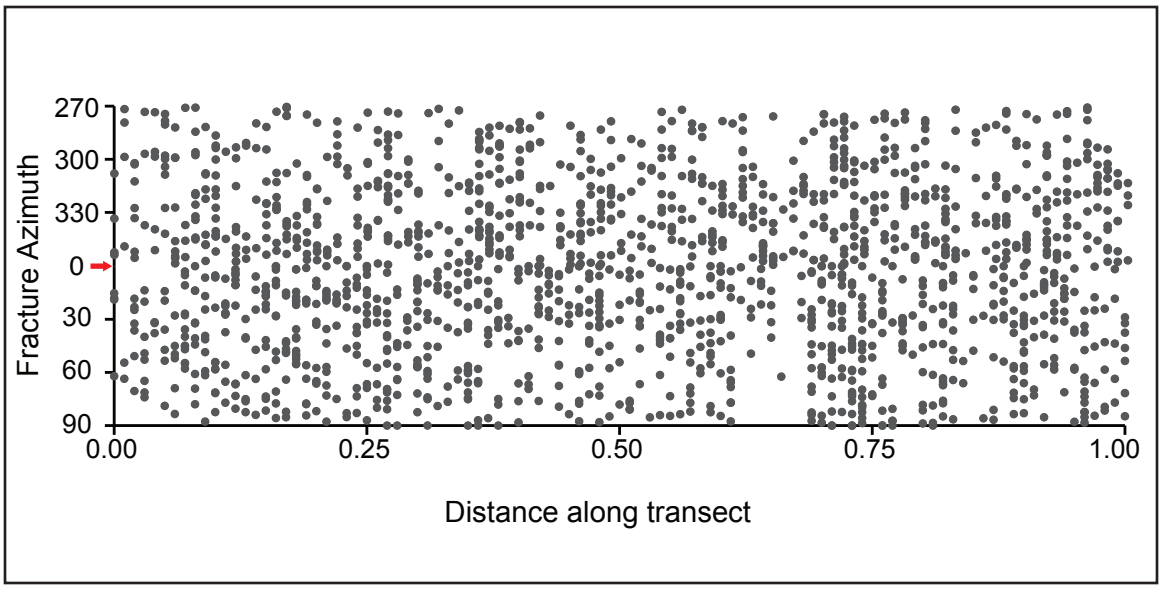

Figure 15. Fracture directions from the transect of sample KH8b-3 plotted with position along the transects, showing the general lack of preferred fracture directions along the length of the transect, or any systematic spatial variation in fracture direction. Fracture data from transects of each sample exhibit a similar pattern and are not shown. The red arrow at 0° indicates the direction of σ_1. Distance is normalized by the length of the transect.

control over the style of deformation or the strength of the sample (Fig. 8). Rather than localizing strain in deformation bands, each sample deformed via distributed particulate flow with some degree of grain damage.

The axially perpendicular open fractures are a curious feature of the deformed samples presented here (Fig. 9). It is difficult to constrain whether these fractures formed during or after the triaxial tests. They may be the result of unloading and handling after running an experiment and during sample processing prior to thin sectioning. Comparable fractures have been observed in samples of similar, poorly lithified sandstones deformed under similar conditions by Skurtveit et al. (2013) who attributed them to unloading and post-test processing. However, the presence of some remaining material in the fractures may suggest that, rather than simple opening fractures, they may be dilational zones—perhaps dilation bands that formed at some stage in the experiment. Considering the difficulty of post-test sample processing, however, it is also conceivable that this material is not in place and was introduced to the fracture during processing. The origin of these fractures therefore remains ambiguous.

Increasing axial strain at the conditions tested here does not appear to have a significant impact on the style of deformation, nor the amount of grain damage in the samples. Strain localization is not apparent in any of the samples, despite applying up to 10% axial strain. The lack of drops in differential stress or evidence of dilation in the volumetric strain data reflect the observed absence of localized shear structures that would accommodate strain by sliding along slip surfaces (Fig. 8ab). However, conducting experiments to higher axial strains could show different behavior with even greater deformation, although from a practical perspective, the amount of applicable axial strain

is limited by the setup of the axial strain gauges in the testing rig. Both differential stress and volumetric strain appear to plateau at higher axial strains. This is perhaps why micro-scale deformation appears similar in each sample. At least under the conditions studied here, a finite amount of grain damage may occur before axial strain is simply accommodated by grain reorganization. However, the amount of grain damage in the samples does increase with the confining pressure applied to the sample, as evidenced by the amount of granular fractures present in KH8b-1, which was deformed at P_{eff} = 20 MPa (Fig. 13). This concurs with the work of Rawling and Goodwin (2003), who infer that more grain fracturing is required for particulate flow to occur at higher confining pressures than at lower ones.

Triaxial deformation experiments have been performed on various types of sandstones, ranging in porosity from 13% to 35% (Wong and Baud, 2012). Those sandstones studied in other experiments are often less porous and better consolidated than the Etchegoin Formation sandstones used in this study. Experimental studies of deformation in unconsolidated sands or poorly lithified sandstones with petrophysical characteristics comparable to the Etchegoin Formation sandstone are not as common in the literature as those focused on more competent rocks (e.g., Chuhan et al., 2002; Rawling and Goodwin, 2003; Skurtveit et al., 2013). The mechanical behavior of the natural coarse-grained sandstone (36% porosity) studied by Skurtveit et al. (2013) most closely resembles that of the Etchegoin Formation sandstone. However, at the same effective confining pressure (5 MPa), despite having similar-shaped stress-strain curves, Skurtveit et al. (2013) observe “diffuse low-angle bands” localized in their sample. These results are also significant because the stress-strain curve does not show any strain-

softening behavior as is sometimes observed associated with deformation band formation (e.g., Menéndez et al., 1996; Mair et al., 2000; Tembe et al., 2008), although the volume strain measured by their strain gauges does show dilation at higher strains than were reached in my experiments (Skurtveit et al., 2013).

Despite the fact that we do observe naturally-occurring deformation bands in the Etchegoin Formation, other triaxial deformation studies on sandstones and computational models suggest that deformation band formation is unlikely in high-porosity sandstones such as those of the Etchegoin Formation (Antonellini and Pollard, 1995). Such sandstones are instead more likely to deform via particulate flow at low stresses, as observed in the deformed samples presented here. Cheung et al. (2012) also report that the high porosity, poorly sorted Boise sandstone did not localize deformation bands during triaxial tests, although natural deformation bands also occur in the Boise sandstone. For the purposes of this study, it therefore appears that triaxial deformation experiments either do not faithfully enough reproduce natural deformation conditions, or deformation bands form under different conditions than those explored in the laboratory.

The question of what stress conditions lead to the development of deformation bands in the Etchegoin Formation sandstone and at what angle to the principle stress directions these will form still remains. Based on the "rolling over" observed in the stress-strain curves, and the grain damage present in the samples, inelastic yielding was achieved in these experiments, but all strain was accommodated by distributed particulate flow. I might expect, based on the results of Tembe et al. (2008) and Skurtveit et al. (2013), that in order to form deformation bands with some shear component (as is commonly observed in the field) in the Etchegoin Formation sandstone under laboratory conditions,

low effective confining pressures would be required. Conversely, higher effective confining pressures would promote the development of compaction bands perpendicular to σ_1 (Tembe et al., 2008). However, the localization of deformation bands at moderate angles to σ_1 is still not apparent in the deformed samples of this study despite low confining pressures.

Perhaps one factor inhibiting the formation of deformation bands in these experiments the relative homogeneity in the samples used. In experiments that successfully produce deformation bands, they at first tend to cluster near the tops and bottoms of samples, likely as a result of local stress heterogeneities (Tembe et al., 2006). Deformation bands likely nucleate as a result of preexisting imperfections within rock masses that act to concentrate stresses and thereby localize features like deformation bands. There are many "impurities" in the Etchegoin Formation, such as fossiliferous layers, that could serve as such nucleation zones. Deformation bands may nucleate within compositionally unique strata before propagating into the surrounding, more homogeneous sandstone layers. The effect of artificially concentrating stresses in triaxial experiments has been explored by Tembe et al. (2006) by imposing circumferential notches on samples prior to tests. As a result of these notches, grain damage and band nucleation occurred a lower stress condition than in unnotched samples (Tembe et al., 2006). Chuhan et al. (2002) also observe in uniaxial tests on sands that grain crushing is more prevalent in lithic sands than in predominately quartz sands, and in coarser sands than finer sands. In the experiments presented here, the relative homogeneity of the samples used may have precluded the development of deformation bands at the stress conditions of the experiments.

Implications for field interpretations

Because deformation bands did not localize in the triaxial deformation experiments, it is impossible to apply these results to understanding how deformation bands form relative to maximum horizontal compressive stress in central California. The low mechanical strength and high porosity of the Etchegoin Formation sandstone, however, does suggest that deformation bands may form at shallow depths. Had the rock unit been buried to greater depths, lower porosity and more widespread grain damage might be expected in the "undeformed" host rock. This shallow burial hypothesis is in agreement with the literature that suggests that deformation bands with shear components will form in porous sandstones at low confining pressures (Tembe et al., 2008; Skurtveit et al., 2013). But, the sample deformed at P_{eff} = 20 MPa is most similar to the naturally deformed sample containing a deformation band. It therefore seems that the Etchegoin Formation must compact significantly before localizing strain, perhaps contradicting the evidence that suggests deformation at low confining pressure.

Potential future work

There are many possibilities to explore in future analysis of the data gathered from this study, as well as in future triaxial deformation experiments to better understand how the Etchegoin Formation accommodates deformation in the San Andreas fault borderlands, and potentially successfully produce and observe deformation bands under laboratory conditions. These include:

- Quantification of grain size distribution. Although beyond the scope of the present study, analyzing the grain size distribution of each deformed sample using ImageJ would supplement the porosity and fracture measurements presented here. A more detailed quantification of the degree of grain crushing present in each deformed sample would also benefit our understanding of the differences in deformation between each sample.
- Investigation of different lithologies. Deformation bands are more prevalent in the field in coarser grained lithologies of the Etchegoin Formation than the one studied here, so future tests might explore differences in experimental behavior between different samples of the Etchegoin Formation.
- Hydrostatic tests. Hydrostatic tests are common in the porous rock deformation literature for establishing the yield stress of a rock – i.e., the point at which it fails by distributed cataclastic flow. These tests increase the mean stresses on samples without applying a differential stress in order to gauge the compactional properties of materials and to serve as a reference for triaxial tests. Such tests may help answer the question of whether more axial strain simply needs to be applied to the cores to induce strain localization, or whether they need to be deformed at altogether different stress conditions.
- True triaxial tests. The tests presented here use the traditional axisymmetric triaxial setup ($\sigma_1 > \sigma_2 = \sigma_3$). But, because deformation bands in the Etchegoin Formation likely form in a three-dimensional stress field, *true triaxial* tests ($\sigma_1 > \sigma_2 > \sigma_3$) would provide a much more accurate simulation of natural conditions in central California.

- Post-test computerized tomographic (CT) imaging of deformed samples or acoustic emission (AE) monitoring. CT imaging of samples after experimental deformation would provide a non-invasive, three-dimensional image of the internal conditions of a sample, which would be particularly useful considering the fragility of the Etchegoin Formation sandstone. This method would help determine whether or not the opening cracks observed here developed during experiments or as a result of post-test sample handling. Monitoring of AE activity during samples is another common method for characterizing the internal behavior of a sample, although AE data are collected over the course of triaxial experiments (e.g., Baud et al., 2004; Tembe et al., 2008). These data allow for reconstructions of where internal deformation takes place within a sample during the experiments, as acoustic emissions are a result of grain breakage and shifting.

CONCLUSIONS

This study presents field measurements of deformation bands from central California and stress interpretations derived from those data, as well as results from triaxial deformation experiments conducted on undeformed samples of the Etchegoin Formation sandstone. The observed discrepancy between S_{Hmax} interpretations derived from deformation bands in central California and S_{Hmax} data from the World Stress Map provides a clear motivation for achieving a better understanding of how to interpret patterns of deformation bands in the Etchegoin Formation. Although these initial experimental results do not yet help with interpretations of the field data, the experiments represent a first step towards understanding how deformation is accommodated in the

Etchegoin Formation in the San Andreas fault system and provide direction for future experiments.

Triaxial deformation experiments conducted on cores of Etchegoin Formation sandstone did not generate deformation bands at effective confining pressures of 20 MPa or 5 MPa and axial strains up to 10%. Samples deformed via distributed particulate flow, and exhibited similar degrees of grain damage and porosity change despite accommodating different amounts of axial strain. These results suggest that the experimental conditions explored here do not reproduce the stress conditions under which natural deformation bands form, or an integral element of strain localization in the Etchegoin Formation is present in the samples used in the present study.

Because of the various geometric patterns in which deformation bands have been observed to develop in different tectonic settings and laboratory experiments, it is important to understand how these features form in the Etchegoin Formation in response to tectonic stresses. Particularly given the Etchegoin Formation's unique petrophysical properties, the results of studies on other sandstones may not be directly applicable to deformation in the Etchegoin Formation. The potential for deformation bands to serve as an independent source of S_{Hmax} measurements in central California to compare against existing datasets highlights the value of these experiments.

ACKNOWLEDGMENTS

I thank my advisors, Sarah Titus at Carleton College and Melodie French at Rice University for their support and guidance throughout the research process. I also thank Sarah Titus for first providing me the opportunity to get involved in this research. I am

further grateful for the support of the Carleton geology faculty and staff, and my peers who have helped me throughout this project. The laboratory work at Rice University in summer 2017 was supported by a Kolenkow Reitz Fellowship awarded through Carleton College.

REFERENCES CITED

Alikarami, R., and Torabi, A., 2015, Micro-texture and petrophysical properties of dilation and compaction shear bands in sand: Geomechanics for Energy and the Environment, v. 3, p. 1–10, doi: 10.1016/j.gete.2015.06.001.

Antonellini, M.A., and Pollard, D.D., 1995, Distinct element modeling of deformation bands in sandstone: Journal of Structural Geology, v. 17, p. 1165–1182, doi: 10.1016/0191-8141(95)00001-T.

Argus, D.F., and Gordon, R.G., 2001, Present tectonic motion across the Coast Ranges and San Andreas fault system in central California: Geological Society Of America Bulletin, v. 113, p. 1580–1592, doi: 10.1130/0016-7606(2001)113.

Aydin, A., and Johnson, A.M., 1978, Development of faults as zones of deformation bands and as slip surfaces in sandstone: Pure and Applied Geophysics, v. 116, p. 931–942. doi: 10.1007/BF00876547.

Aydin, A., and Johnson, A.M., 1983, Analysis of faulting in porous sandstones: Journal of Structural Geology, v. 5, p. 19–31, doi: 10.1016/0191-8141(83)90004-4.

Ballas, G., Soliva, R., Benedicto, A., and Sizun, J.P., 2014, Control of tectonic setting and large-scale faults on the basin-scale distribution of deformation bands in porous sandstone (Provence, France): Marine and Petroleum Geology, v. 55, p. 142–159, doi: 10.1016/j.marpetgeo.2013.12.020.

Bartow, J.A., 1988, The Cenozoic evolution of the San Joaquin Valley, California: U.S. Geological Survey Professional Paper 1501, 40 p.

Baud, P., Klein, E., and Wong, T. fong, 2004, Compaction localization in porous sandstones: Spatial evolution of damage and acoustic emission activity: Journal of Structural Geology, v. 26, p. 603–624, doi: 10.1016/j.jsg.2003.09.002.

Bésuelle, P., Desrues, J., and Raynaud, S., 2000, Experimental characterisation of the localisation phenomenon inside a Vosges sandstone in a triaxial cell: International Journal of Rock Mechanics and Mining Sciences, v. 37, p. 1223–1237, doi: 10.1016/S1365-1609(00)00057-5.

Brune, J.N., Henyey, T.L., and Roy, R.F., 1969, Heat flow, stress, and rate of slip along the San Andreas Fault, California: Journal of Geophysical Research, v. 74, p. 3821–3827, doi: 10.1029/JB074i015p03821.

Cheung, C.S.N., Baud, P., and Wong, T.F., 2012, Effect of grain size distribution on the development of compaction localization in porous sandstone: Geophysical Research Letters, v. 39, p. 6–10, doi: 10.1029/2012GL053739.

Cilona, A., Baud, P., Tondi, E., Agosta, F., Vinciguerra, S., Rustichelli, A., and Spiers, C.J., 2012, Deformation bands in porous carbonate grainstones: Field and laboratory observations: Journal of Structural Geology, v. 45, p. 137–157, doi: 10.1016/j.jsg.2012.04.012.

Eichhubl, P., Hooker, J.N., and Laubach, S.E., 2010, Pure and shear-enhanced compaction bands in Aztec Sandstone: Journal of Structural Geology, v. 32, p. 1873–1886, doi: 10.1016/j.jsg.2010.02.004.

Fossen, H., Schultz, R.A., Shipton, Z.K., and Mair, K., 2007, Deformation bands in sandstone: a review: Journal of the Geological Society, v. 164, p. 755–769, doi: 10.1144/0016-76492006-036.

Fossen, H., Schultz, R.A., and Torabi, A., 2011, Conditions and implications for compaction band formation in the Navajo Sandstone, Utah: Journal of Structural Geology, v. 33, p. 1477–1490, doi: 10.1016/j.jsg.2011.08.001.

Handin, J., and Hager, R. V., 1974, Experimental Deformation of Sedimentary Rocks Under Confining Pressure: Tests at Room Temperature on Dry Samples: v. 41, p. 1-50.

Handin, J., Hager, R. V., Friedman, M., and Feathers, J.N., 1963, Experimental Deformation of Sedimentary Rocks under Confining Pressure: Pore Pressure Tests: American Association of Petroleum Geologists Bulletin, v. 47, p. 717–755.

Hardebeck, J.L., and Hauksson, E., 1999, Role of fluids in faulting inferred from stress field signatures: Science, v. 285, p. 236–239, doi: 10.1126/science.285.5425.236.

Hardebeck, J.L., and Michael, A.J., 2004, Stress orientations at intermediate angles to the San Andreas Fault, California: Journal of Geophysical Research: Solid Earth, v. 109, p. 1–16, doi: 10.1029/2004JB003239.

Harding, T.P., 1976, Tectonic Significance and Hydrocarbon Trapping Consequences of Sequential Folding Synchronous with San Andreas Faulting, San Joaquin Valley, California: American Association of Petroleum Geologists Bulletin, v. 60, p. 356–378.

Heidbach, O., Tingay, M., Barth, A., Reinecker, J., Kurfeß, D., and Müller, B., 2008, The World Stress Map database release 2008, doi:10.1594/GFZ.WSM.Rel2008.

Jamison, W.R., and Stearns, D.W., 1982, Tectonic deformation of Wingate Sandstone, Colorado National Monument.: American Association of Petroleum Geologists Bulletin, v. 66, p. 2584–2608.

Klimczak, C., Soliva, R., Schultz, R.A., and Chéry, J., 2011, Sequential growth of deformation bands in a multilayer sequence: Journal of Geophysical Research: Solid Earth, v. 116, p. 1–14, doi: 10.1029/2011JB008365.

Lettis, W.R., and Hanson, K.L., 1991, Crustal strain partitioning: implications for seismic-hazard assessment in western California: Geology, v. 19, p. 559–562.

Lindquist, P.C., Newman, A.C., Livesay, L., and Titus, S.J., 2016, Deformation bands in the Etchegoin Formation of central California: Implications for stress orientations NE of the San Andreas fault, American Geophysical Union Fall Meeting.

Livesay, L., Newman, A.C., Yourd, A.R., and Titus, S.J., 2013, Deformation bands in the Etchegoin Formation at Parkfield: Implications for stresses on the San Andreas fault in central California, Geological Society of America Fall Meeting.

Loomis, K.B., 1990, Depositional environments and sedimentary history of the Etchegoin Group, west-central San Joaquin Valley, California, *in* Structure, Stratigraphy and Hydrocarbon Occurrences of the San Joaquin Basin, California, 1990, Pacific Section of AAPG, p. 231–246.

Medwedeff, D.A., 1989, Growth Fault-Bend Folding at Southeast Lost Hills, San Joaquin Valley, California: American Association of Petroleum Geologists Bulletin, v. 73, p. 54–67.

Menéndez, B., Zhu, W., and Wong, T., 1996, Micromechanics of brittle faulting and cataclastic flow in Berea sandstone: Journal of Structural Geology, v. 18, p. 1–16.

Mollema, P.N., and Antonellini, M.A., 1996, Compaction bands: a structural analog for anti-mode I cracks in aeolian sandstone: Tectonophysics, v. 267, p. 209–228.

Mount, V.S., and Suppe, J., 1977, State of stress near the San Andreas fault : Implications for wrench tectonics: Geology, p. 1143–1146.

Namson, J.S., and Davis, T.L., 1988, Seismically active fold and thrust belt in the San Joaquin Valley , central California: Geological Society Of America Bulletin, v. 100, p. 257–273.

Newman, A. C., 2011, Using small-scale structures as a tool for understanding regional deformation: A study of deformation bands and faults at Kettleman Hills, California [B.A. thesis]: Carleton College, 39 p.

Rasband, W.S., ImageJ, U. S. National Institutes of Health, Bethesda, Maryland, USA, https://imagej.nih.gov/ij/, 1997-2016.

Rawling, G.C., and Goodwin, L.B., 2003, Cataclasis and particulate flow in faulted, poorly lithified sediments: Journal of Structural Geology, v. 25, p. 317–331.

Reches, Z., 1983, Faulting of rocks in three-dimensional strain field II. Theoretical analysis: v. 95, p. 133–156.

Scholz, C.H., 1993, Evidence for a strong San Andreas fault: Geology, v. 28, p. 163–166.

Schultz, R.A., and Siddharthan, R., 2005, A general framework for the occurrence and faulting of deformation bands in porous granular rocks: Tectonophysics, v. 411, p. 1–18, doi: 10.1016/j.tecto.2005.07.008.

Skurtveit, E., Torabi, A., Gabrielsen, R.H., and Zoback, M.D., 2013, Experimental investigation of deformation mechanisms during shear-enhanced compaction in poorly lithified sandstone and sand: Journal of Geophysical Research, v. 118, p. 4083–4100, doi: 10.1002/jgrb.50342.

Tembe, S., Baud, P., and Wong, T., 2008, Stress conditions for the propagation of discrete compaction bands in porous sandstone: Journal of Geophysical Research, v. 113, p. 1–16, doi: 10.1029/2007JB005439.

Tembe, S., Vajdova, V., Wong, T., and Zhu, W., 2006, Initiation and propagation of strain localization in circumferentially notched samples of two porous sandstones: Journal of Geophysical Research, v. 111, p. 1–20, doi: 10.1029/2005JB003611.

Teyssier, C., Tikoff, B., and Markley, M., 1993, Oblique plate motion and continental tectonics: Geology, v. 23, p. 447–450.

Titus, S.J., Demets, C., and Tikoff, B., 2006, Thirty-Five-Year Creep Rates for the Creeping Segment of the San Andreas Fault and the Effects of the 2004 Parkfield Earthquake: Constraints from Alignment Arrays, Continuous Global Positioning System, and Creepmeters: Bulletin of the Seismological Society of America, v. 96, p. 250–268, doi: 10.1785/0120050811.

Titus, S.J., Dyson, M., DeMets, C., Tikoff, B., Rolandone, F., and Bürgmann, R., 2011, Geologic versus geodetic deformation adjacent to the San Andreas fault, central California: Geological Society Of America Bulletin, v. 123, p. 794–820, doi: 10.1130/B30150.1.

Torabi, A., and Fossen, H., 2009, Spatial variation of microstructure and petrophysical properties along deformation bands in reservoir sandstones: American Association of Petroleum Geologists Bulletin, v. 93, p. 919–938, doi: 10.1306/03270908161.

Townend, J., and Zoback, M.D., 2004, Regional tectonic stress near the San Andreas fault in central and southern California: Geophysical Research Letters, v. 31, p. 1–5, doi: 10.1029/2003GL018918.

Townend, J., and Zoback, M.D., 2001, Implications of earthquake focal mechanisms for the frictional strength of the San Andreas fault system, *in* Holdsworth, R.E., Strachan, R.A., Magloughlin, J.F., and Knipe, R.J. eds., The Nature and Tectonic Significance of Fault Zone Weakening, London, Geological Society of London, p. 13–21.

Wentworth, C.M., and Zoback, M.D., 1989, The style of Late Cenozoic deformation at the easter front of the California Coast Ranges: Tectonics, v. 8, p. 237–246.

Wong, T., and Baud, P., 2012, The brittle-ductile transition in porous rock: A review: Journal of Structural Geology, v. 44, p. 25–53, doi: 10.1016/j.jsg.2012.07.010.

Wong, T., Baud, P., and Klein, E., 2001, Localized failure modes in a compactant porous rock: Geophysical Research Letters, v. 28, p. 2521–2524.

Woodring, W. P., Stewart, R. B., and Richards, R. W., 1940, Geology of the Kettleman Hills oil field, California; stratigraphy, paleontology, and structure: U.S. Geological Survey Professional Paper 195, 170 p.

Zhang, J., Wong, T., and Davis, D.M., 1990, Micromechanics of Pressure-Induced Grain Crushing in Porous Rocks: Journal of Geophysical Research, v. 95, p. 341–352.

Zoback, M.D., Zoback, M. Lou, Mount, V.S., Suppe, J., Eaton, J.P., Healy, J.H., Oppenheimer, D., Reasenberg, P., Jones, L., Raleigh, C.B., Wong, I.G., Scotti, O., and Wentworth, C.M., 1987, New Evidence on the State of Stress of the San Andreas Fault System: Science, v. 238, p. 1105–1111.